HHS Public Access

Author manuscript

Cell Rep. Author manuscript; available in PMC 2024 June 12.

Published in final edited form as:

Cell Rep. 2024 April 23; 43(4): 113970. doi:10.1016/j.celrep.2024.113970.

Long-range inhibitory neurons mediate cortical neurovascular coupling

Catherine F. Ruff[1,6], **Fernanda Juarez Anaya**[1,6], **Samuel J. Dienel**[2], **Adiya Rakymzhan**[3], **Alain Altamirano-Espinoza**[3], **Jonathan J. Couey**[1], **Mitsuhiro Fukuda**[5], **Alan M. Watson**[4], **Aihua Su**[1], **Kenneth N. Fish**[2], **Maria E. Rubio**[1], **Bryan M. Hooks**[1], **Sarah E. Ross**[1,*], **Alberto L. Vazquez**[3,5,7,*]

[1]Department of Neurobiology, University of Pittsburgh, Pittsburgh, PA, USA

[2]Department of Psychiatry, University of Pittsburgh, Pittsburgh, PA, USA

[3]Department of Bioengineering, University of Pittsburgh, Pittsburgh, PA, USA

[4]Center for Biologic Imaging, University of Pittsburgh, Pittsburgh, PA, USA

[5]Department of Radiology, University of Pittsburgh, Pittsburgh, PA, USA

[6]These authors contributed equally

[7]Lead contact

SUMMARY

To meet the high energy demands of brain function, cerebral blood flow (CBF) parallels changes in neuronal activity by a mechanism known as neurovascular coupling (NVC). However, which neurons play a role in mediating NVC is not well understood. Here, we identify in mice and humans a specific population of cortical GABAergic neurons that co-express neuronal nitric oxide synthase and tachykinin receptor 1 (Tacr1). Through whole-tissue clearing, we demonstrate that Tacr1 neurons extend local and long-range projections across functionally connected cortical areas. We show that whisker stimulation elicited Tacr1 neuron activity in the barrel cortex through feedforward excitatory pathways. Additionally, through optogenetic experiments, we demonstrate that Tacr1 neurons are instrumental in mediating CBF through the relaxation of mural cells in a similar fashion to whisker stimulation. Finally, by electron microscopy, we observe that Tacr1 processes contact astrocytic endfeet. These findings suggest that Tacr1 neurons integrate cortical activity to mediate NVC.

*Correspondence: saross@pitt.edu (S.E.R.), alv15@pitt.edu (A.L.V.).

AUTHOR CONTRIBUTIONS

Conceptualization, C.F.R., S.E.R., and A.L.V.; methodology, C.F.R., F.J.A., S.J.D., S.E.R., and A.L.V.; investigation, C.F.R., F.J.A., A.R., S.J.D., A.A.-E., M.F., J.C., A.S., and A.L.V.; formal analysis, C.F.R., F.J.A., A.R., and A.L.V.; writing – original draft, C.F.R., F.J.A., S.E.R., and A.L.V.; writing – review & editing, F.J.A., S.E.R., and A.L.V.; funding, C.F.R., F.J.A., S.J.D., A.M.W., K.N.F., M.E.R., B.M.H., S.E.R., and A.L.V.; supervision, S.E.R. and A.L.V.

SUPPLEMENTAL INFORMATION

Supplemental information can be found online at https://doi.org/10.1016/j.celrep.2024.113970.

DECLARATION OF INTERESTS

The authors declare no competing interests.

In brief

Ruff et al. identify a subpopulation of inhibitory neurons, Tacr1 neurons, that regulate cerebral blood flow. Tacr1 neurons are long-range-projecting neurons that use feedforward excitatory pathways to mediate neurovascular coupling.

Graphical Abstract

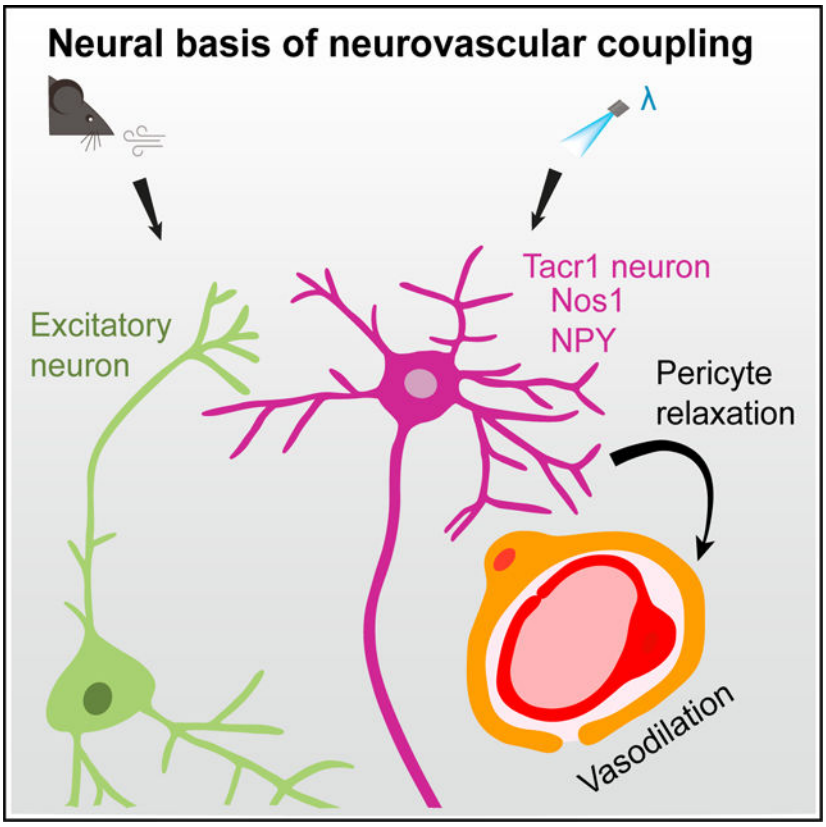

INTRODUCTION

Neurovascular coupling (NVC) is the mechanism that translates local neural activity into precise adjustments in local cerebral blood flow (CBF) through the modulation of upstream vessel diameter.[1] The changes in blood flow driven by NVC are routinely used in brain imaging methodologies to examine brain function (i.e., blood-oxygen-level-dependent [BOLD] fMRI imaging). Furthermore, NVC dysfunction is associated with the pathogenesis of neurodegenerative diseases, such as Alzheimer's disease (AD).[2,3] In neurodegenerative diseases, NVC dysfunction leads to changes in CBF that impair cognitive function.[4–6] For example, in AD, amyloid-b accumulation leads to the degeneration of smooth muscle cells and pericytes, resulting in reduced CBF, which contributes to cognitive decline.[7] Thus, the proper functioning of NVC is critical for normal brain function.

NVC involves coordinated activity across multiple cell types, including neurons, astrocytes, vascular smooth muscle cells (VSMCs), pericytes, and endothelial cells.[2,5,8] Given the

importance of NVC in maintaining brain health, there is great interest in identifying specific neuronal cell types that drive hemodynamic responses. Neurons that express neuronal nitric oxide synthase (Nos1, also known as nNOS) are widely assumed to be involved in NVC,[1,9] given that nitric oxide (NO), a potent vasodilator, is a key signaling molecule involved in mediating NVC.[10–14] There is strong pharmacological evidence that inhibition of Nos reduces neural-evoked changes in blood flow.[15–17] Cortical nNOS neurons are divided into two subtypes, type I and type II, based on morphology and dihydronicotinamide adenine dinucleotide phosphate diaphorase staining intensity.[18,19] Type I nNOS neurons express higher levels of Nos1 and co-express tachykinin receptor 1 (Tacr1), also known as substance P receptor, in all species evaluated (mice, rats, and nonhuman primates).[18] Tacr1 neurons are a small population concentrated in layers 5/6 and represent approximately 2% of total GABAergic neurons in the cortex.[19] Several studies now show that activation of nNOS neurons is strongly correlated with vascular responses and that pharmacological interventions targeting substance P receptors result in changes in blood flow.[11,20–23] Altogether, these features make Tacr1 neurons ideally poised to modulate blood flow.[24] However, the extent to which Tacr1 neurons contribute to NVC, compared to other Nos1 neurons, is unknown.

NVC requires that an electrical neural signal be translated into a hemodynamic response, but how neurons communicate their energy needs to blood vessels is only partially understood. One of the remaining controversies is the location(s) of the microvascular tree at which this regulation occurs.[25] One possibility is that NVC is mediated by the relaxation of VSMCs, which regulate changes in the diameter of penetrating arterioles. VSMCs are thought to be better candidates than pericytes since several reports have suggested that pericytes are passive and do not contribute to blood flow response induced by neural activity.[26,27] The idea that pericytes are passive gained further acceptance based on findings from studies using genetic and imaging tools, as well as single-cell RNA sequencing demonstrating that pericytes do not express alpha-smooth muscle actin, an essential protein for smooth muscle contraction.[27,28] However, other studies have concluded that a type of pericytes, ensheathing pericytes, are contractile and control CBF through the regulation of capillary diameter.[29–34] These ensheathing pericytes are found proximal to branches of penetrating arteriole offshoots, a region sometimes referred to as precapillary arteriole or the arteriole-to-capillary transition zone. Investigating whether ensheathing pericytes play a prominent role in NVC is important since it has implications for the interpretation of the BOLD signal associated with human brain imaging.

In this study, we build on our previous work that characterized the contribution of inhibitory neurons in blood flow regulation.[21] We used *Tacr1*^{CreER} knockin allele mice[35] together with a combination of *in vivo* laser Doppler flowmetry (LDF), *in vivo* two-photon (2P) Ca^{2+} imaging, *in vitro* assays, and electron microscopy to detail the anatomical and functional properties of Tacr1 neurons. This study characterizes Tacr1 neurons as strong mediators of NVC.

RESULTS

Tacr1 neurons are sparse and have similar expression profiles in mouse and human

To determine the genetic profile of Tacr1 neurons, we performed a combination of multiplex fluorescence *in situ* hybridization (FISH) and immunohistochemistry (IHC) in mouse and human cortices (see STAR Methods). Recent single-cell sequencing studies have suggested that Nos1 is expressed in a well-defined transcriptomic subset of GABAergic neurons.[16,36] Using FISH, we identified and characterized this population in mouse cortex as a somatostatin (SST)-expressing subpopulation that showed an almost complete overlap of three markers: *Nos1*, *Tacr1*, and *Chodl* (Figures 1A, 1C, S1A, S1D, and S1E). In human cortex, we likewise observed that a small subpopulation of *SST*-positive neurons co-expressed *NOS1*, *TACR1*, and *CHODL* (Figures 1D, S1A, and S1F–S1H). In addition, we observed that Tacr1 neurons were similarly sparse in superficial cortical layers and more concentrated in layer 5/6 and white matter (Figures 1B, 1E, S1B, and S1C). To visualize these neurons and examine their vasoregulatory role in more detail, our laboratory generated a $Tacr1^{CreER}$ knockin allele targeting type 1 nNOS neurons without disrupting the Nos1 locus. This allele faithfully recapitulated the endogenous expression of Tacr1 at the levels of both protein and mRNA and successfully targeted the majority of neurons that express Nos1 at high levels.[35] To assess the efficiency and specificity of recombination in the brain, we crossed $Tacr1^{CreER}$ mice to mice harboring a Cre-dependent tdTomato (tdT) fluorescent reporter (Figure 1F). Immunohistological assessment of cortical tissue from $Tacr1^{CreER}$-*tdT* mice shows that tdT is expressed in 84% of labeled neurons and that 95% of tdT-positive neurons expressed Nos1 (Figures 1G, 1H, S2, and S3). These findings are consistent with previous descriptions of type 1 nNOS neurons in guinea pigs, rats, and monkeys and strongly suggest conservation of this cell type across species.[15]

Tacr1 neurons extend projections to ipsilateral and contralateral hemispheres

Until recently, cortical GABAergic neurons were generally considered to be interneurons in which axons only project a short distance from their soma. Although most GABAergic neurons have axons that reside in the same structure as their soma, there are GABAergic neurons that have long-range axons and project to different brain regions. For example, there is some evidence suggesting that Tacr1 neurons may extend long-range (>1.5 mm) axonal projections.[38] To visualize the morphology of these neurons, we performed Cre-dependent retrograde viral labeling (AAVrg-DIO-YFP; see STAR Methods) in the primary somatosensory cortex (S1) of $Tacr1^{CreER}$ mice combined with either IHC or whole-tissue clearing and ribbon scanning confocal microscopy (Figures 1I, S4A, and S4D). Labeled soma were widely distributed across the cortex, consistent with the idea that Tacr1 neurons have long-range projections that extend within and across hemispheres (Figures 1J, 1K, S4B, S4C, S4E, and S4F). Moreover, interhemispheric projections from Tacr1 neurons dominated the homotopic S1, paralleling known pyramidal cortico-cortical connections in the contralateral cortex (Figure 1K). Single-cell tracing revealed that dendrites from Tacr1 neurons have extensive radial branches extending ~500 μm from the soma, whereas axons from Tacr1 neurons had limited branching and extended several millimeters (Figures 1L, 1M, and S4G). Our findings confirm that Tacr1 neurons have long-distance (>1.5 mm) cortico-cortical projections to both ipsilateral and contralateral hemispheres.

Tacr1 neurons receive excitatory input

To begin investigating the functional role of cortical Tacr1 neurons in NVC, we examined whether these neurons respond to sensory stimulation using 2P microscopy in awake, head-fixed *Tacr1*^{CreER} mice expressing GCaMP6f (Figure 2A). We generally observed 4–12 GCaMP-expressing Tacr1 neurons in the whisker S1 over an imaging volume spanning 350 ×350 ×300 μm, consistent with the idea that these neurons are sparse. Several planes with at least one neuron were imaged during whisker stimulation (50 ms puffs delivered at 5 Hz for 1 s every 30 s; see STAR Methods). These experiments showed a rapid and robust Ca^{2+} transient in Tacr1 neurons in the contralateral barrel cortex (Figures 2B–2D). For comparison, we also conducted separate experiments in Thy1-GCaMP6s mice to examine cortical excitatory neuron responses. These experiments showed similar Ca^{2+} dynamics in pyramidal neurons upon the same whisker stimulation paradigm (Figure 2B). To investigate the synaptic basis of this evoked activity, we performed subcellular channelrhodopsin-2 (ChR2)-assisted circuit mapping *in vitro* experiments in *Tacr1*^{CreER}-*tdT* mice in either pyramidal neurons or thalamic neurons expressing ChR2 (Figure 2E). Recordings from Tacr1 neurons expressing tdT in the cortex during optogenetic simulation of either pyramidal neurons or thalamic neurons in the presence of tetrodotoxin and 4-aminopyridine evoked clear postsynaptic currents in Tacr1 neurons (Figures 2F and 2G). This finding is consistent with monosynaptic cortico-cortical and thalamocortical excitatory input. Thus, Tacr1 neurons can integrate local activity through feedforward excitatory pathways from the cortex and thalamus.

Optogenetic manipulation of Tacr1 neurons increases CBF

To test the role of Tacr1 neurons in vasodilation, we conducted awake, head-fixed experiments in *Tacr1*^{CreER} mice expressing ChR2 (*Tacr1*^{CreER} mice were bred with Ai32 mice to drive the expression of ChR2 in Tacr1 neurons). Our group has previously titrated optogenetic stimulation parameters for NVC studies that aimed to activate neurons throughout cortical layers while avoiding vascular responses due to the optogenetic stimulus by itself.[39] We used these optogenetic stimulation parameters and concurrently measured changes in CBF using LDF (Figures 2H, S5A, and S5D). Although Tacr1 neurons are sparse, approximately 2% of cortical neurons, their optogenetic activation in the whisker S1 significantly increased CBF relative to prestimulation levels (Figures 2I–2K). This increase in CBF was comparable to that observed upon whisker stimulation measured in the same mice from the same region (Figure S5G). In contrast, blue light stimulation did not elicit a CBF response in ChR2-negative animals, in agreement with our previous control experiments (Figures S5H–S5N). Moreover, we tested optogenetic stimulation (1 mW, 1 s, 5 Hz) of Tacr1 neurons during different pulse durations (2, 10, and 30 ms) as well as optogenetic stimulation (1 mW, 1 s, 10 ms) at different frequencies (5, 10, 20, and 40 Hz) (Figures S5B, S5C, S5E, and S5F). CBF increased both as a function of increasing the stimulation pulse duration at 5 Hz or the stimulation frequency to 10 and 20 Hz. These results show an energy-dependent effect for optogenetic stimulation of Tacr1 neurons on CBF.

To further address the role of Tacr1 neurons for NVC, we tested whether inhibition of Tacr1 neurons in the S1 reduces the hemodynamic response to whisker stimulation (Figure 2L). To

this end, we conducted similar experiments in *Tacr1*^{CreER} mice bred with Ai40 mice to drive the expression of ArchT in Tacr1 neurons for optogenetic inhibition. Indeed, the whisker-evoked NVC response was significantly reduced upon optogenetically mediated inhibition of Tacr1 neurons (Figures 2M–2O and S6A– S6C). In contrast, optogenetic stimulation alone in control mice did not elicit a CBF response and had no effect on the whisker-evoked CBF response (Figures S6D–S6H). To test whether the whisker-evoked CBF changes were nNOS dependent, we infused an nNOS inhibitor—Nω-propyl-L-arginine (L-NPA)—into the cortex. As expected, L-NPA significantly reduced the whisker-evoked CBF responses compared to vehicle (Figures 2P and 2R). Moreover, the reduction upon inhibition of Tacr1 neurons or nNOS was similar in magnitude (~40%). These findings are consistent with the notion that Tacr1 neurons are strong mediators of vasodilation via the release of NO.

Tacr1 neurons mediate NVC via ensheathing pericytes and arteriolar VSMCs

An unresolved question is whether NVC is initiated by the relaxation of VSMCs or ensheathing pericytes.[26,29,32,33] To investigate the site of NVC within the neurovascular tree, we monitored mural cell activity and cortical blood vessel diameter using 2P microscopy through cortical windows in awake, head-fixed mice. (Figures 3A and 3B). We bred double-transgenic mice that express ChR2 in Tacr1 neurons and GCaMP6f in mural cells (VSMCs and pericytes) (Figure S7A). The vasculature was visualized using an intravascular dye to measure vascular responses as changes in vessel diameter. We classified a capillary as a small (<10 μm in diameter) intracortical vessel that was located one to four branch orders from the penetrating arteriole. A mural cell was classified as an ensheathing pericyte if it had a ring-like morphology surrounding a capillary (Figure 3C). We found that optogenetic activation of cortical Tacr1 neurons resulted in a transient decrease in cytosolic calcium ($[Ca^{2+}]_i$) in both pericytes and VSMCs, consistent with relaxation (Figures 3D and 3E). This relaxation was accompanied by vasodilation of both arterioles and capillaries (Figure 3F, S7B, and S7C). We next compared the kinetics of relaxation between VSMCs of parenchymal arterioles and nearby ensheathing pericytes (Figure S7D). For both optogenetic stimulation and whisker stimulation, the average onset of the responses was similar for the diameter of capillaries and arterioles as well as pericyte calcium and VSMC calcium. Importantly, we observed no differences in the kinetics of vasodilation between optogenetic activation and whisker stimulation (Figures 3G and 3H). These findings are consistent with the idea that Tacr1 neurons are active participants in NVC. Since we did not observe measurable vasodilation in deeper capillaries with thin-stranded pericytes, these findings suggest that vessels with ensheathing pericytes and arteriolar smooth muscle cells are primary sites of early vasoregulation and that Tacr1 neurons engage these mural cells to mediate vasodilation.

Tacr1 neuron processes contact astrocytes

Based on our findings that Tacr1 neurons regulate CBF, we hypothesized that Tacr1 neuronal processes contact the neurovascular unit. To visualize the ultrastructure of Tacr1 neurons in the context of the neurovascular unit and the possibility of contacts between Tacr1 neuron processes and vascular elements, we used transmission electron microscopy of immunolabeled Tacr1 neurons that expressed ChR2. We found that both presynaptic and postsynaptic terminals of Tacr1 neurons make contacts with astrocytes and/or astrocytic

endfeet that surround blood vessels (Figures 3I, 3J, and S8). Moreover, we observed the juxtaposition of an astrocytic endfoot to the asymmetrical synapse between a putative excitatory presynaptic terminal and a Tacr1 neuron postsynaptic terminal (Figure 3I). These observations provide anatomical evidence for the idea that glutamate release from an excitatory neuron might elicit the postsynaptic synthesis of NO from Tacr1 neurons to cause vasodilation. Intriguingly, we found that both the presynaptic (axonal) terminals and the postsynaptic (dendritic) processes of Tacr1 neurons are intimately associated with the neurovascular unit and thus anatomically positioned to mediate NVC (Figure 3K).

DISCUSSION

In summary, we found that cortical Tacr1 neurons are a distinct GABAergic neural population with long-range projections. These cells co-express Sst, Nos1, and Chodl in both mouse and human cortices. Our study suggests that Tacr1 neurons mediate feedforward increases in CBF in the barrel cortex that are recruited by whisker stimulation. Activation of cortical Tacr1 neurons caused the relaxation of mural cells, as evidenced by the decrease in $[Ca^{2+}]_i$, that was accompanied by the vasodilation of arterioles and capillaries. Finally, our anatomical data indicated that Tacr1 neurons contact the neurovascular unit through both their dendrites and their axons.

Using *Tacr1*^{CreER} mice, we found that optogenetic activation of surprisingly few neurons elicited significant vasodilation and that sensory-evoked vascular responses were reduced when Tacr1 neurons were optogenetically inhibited. Moreover, we found that inhibition of nNOS reduces the sensory-evoked whisker responses, consistent with previous results using nonselective Nos inhibitors.[40–43] These findings position Tacr1 neurons as a key neuronal source of NO for functional hyperemia in the cortex. Although these findings strongly suggest that Tacr1 neurons play in important role in NVC, we acknowledge that this neuronal population is not the only one that influences CBF. Pyramidal cells are known to play a role via the release of prostaglandins.[44] In addition, we and others have shown that optogenetic stimulation of parvalbumin (PV) and SST neurons also have hemodynamic effects.[21,22] However, the temporal dynamics of Tacr1-neuron-evoked changes, which are immediate and transient, are most similar to those observed in response to sensory stimulation, in both shape and amplitude (Figures 2H–2O). In contrast, the stimulation-induced blood flow changes following activation of PV neurons are very slow, and the changes observed in response to activation of SST neurons are multiphasic. Thus, we favor the possibility that Tacr1 neurons are a dominant neuronal cell type that mediates NVC.

Our study revealed that Tacr1 neurons receive excitatory input from both pyramidal neurons and thalamocortical neurons. In addition, Tacr1 neurons are known to receive cholinergic input from the basal forebrain[45] and respond to substance P,[18] which is released from PV interneurons.[46] Thus, Tacr1 neurons are well positioned to anticipate metabolic needs. One of the interesting features of Tacr1 neurons that we elucidated in this study is that Tacr1 neurons extend long-range projections across functionally connected cortical regions. At this stage, we do not know whether these long-range axonal projections are involved in regulating blood flow. However, this is an attractive possibility because blood flow changes

observed in fMRI studies typically show bilateral homotopic changes across hemispheres.[47–50] The long-range projections from Tacr1 neurons could contribute, through feedforward mechanisms, to the changes in blood flow that are observed between functionally connected hemispheric regions.

An unresolved question is whether pericytes can actively vasodilate to modulate rapid CBF changes. Several studies suggest that most pericytes are passive cells and do not contribute to blood flow responses induced by neuronal activity.[26,27] However, other studies have concluded that pericytes can be contractile and control blood flow by regulating capillary diameter.[33] Some of this controversy is because there are several distinct types of pericytes, which may have different functional roles.[32,51] There is now converging evidence that a particular subtype of pericytes—ensheathing pericytes—are selectively involved in blood flow regulation.[52–54] We found that activation of Tacr1 neurons caused a rapid decrement in the $[Ca^{2+}]_i$ in ensheathing pericytes that occurred in a similar time frame to that observed in VSMCs. In addition, the kinetics were similar to those observed upon whisker stimulation. These findings suggest that vessels with ensheathing pericytes and arteriolar smooth muscle cells are primary sites of early vasoregulation.

Several studies have reported that neurons first signal to astrocytes, which then signal to VSMCs or other contractile cells to mediate NVC. These studies have largely focused on glutamate, released from excitatory neurons, activating metabotropic glutamate receptors 1 and 5 on astrocytes.[55] Our study complements this work by suggesting a parallel pathway through which neuronal activity in excitatory neurons could result in vasodilation. Our data indicate that pyramidal cells activate Tacr1 neurons and that Tacr1 neurons make direct contact with the neurovascular unit. This proximity positions Tacr1 neurons to modulate mural cell contractility via NO, even when considering the diffusion kinetics of this gas.[36,56] Our anatomical data also suggest that cortical Tacr1 neurons may signal to astrocytes. The juxtaposition of an astrocytic endfoot to the symmetrical synapse between an excitatory presynaptic terminal and a Tacr1 postsynaptic terminal is suggestive of a tripartite synapse. The tripartite synapse represents a unique synapse physiology involving the multidirectional communication between neurons and astrocytes.[57,58] The functional details of this complex (termed the ‘‘neuronal-astrocytic-vascular tripartite functional unit’’) are not entirely known, but it is suspected that this interaction facilitates the release of vasoactive mediators, such as NO, to elicit a hemodynamic response. The finding that Tacr1 neurons form a tripartite synapse is consistent with previous observations indicating that glutamate triggers NO release and is consistent with a direct NO-mediated mechanism for mural cell relaxation and subsequent vasodilation. Moreover, these findings raise the intriguing possibility that NVC might occur within subdomains of the Tacr1 dendritic tree, thereby enabling highly localized control of blood flow. Given the association between impaired NVC and neurodegenerative diseases, it will be essential to investigate whether dysfunction in Tacr1 neurons contributes to disease pathogenesis.

Although our study was motivated by the potential vasodilatory role of Tacr1 neurons because they express high levels of Nos1, this population also expresses high levels of neuropeptide Y (NPY), which is a vasoconstricting agent. Previous studies have suggested that sensory stimulation induces arteriolar dilation followed by constriction and that the

constriction phase is mediated by NPY.[59] In our studies, brief optogenetic stimulation of Tacr1 neurons did not produce vasoconstriction following dilation. However, we speculate that different stimulation parameters might reveal a role for Tacr1 neurons in vessel constriction.

Intriguingly, Tacr1 neurons are known to be sleep active, and their activity is thought to promote the delta rhythms characteristic of slow-wave sleep.[60–62] In addition, these neurons receive input from hypocretin/orexin-expressing neurons in the hypothalamus that are involved in the regulation of sleep.[63] At this stage, we do not know the connection between the activity of Tacr1 neurons during slow-wave sleep and their vasoregulatory role. In this regard, it is noteworthy that vascular dynamics are modulated in a sleep-cycle-dependent manner,[64–66] potentially involving a role of Tacr1 neurons in this process.

Limitations of the study

Although our findings highlight a significant role for Tacr1 neurons in cortical NVC, we note that there are several limitations to our study. In particular, we acknowledge that Tacr1 neurons are likely just one of the neuronal populations that are involved in the regulation of blood flow. In addition, while the idea that Tacr1 neurons mediate vasodilation directly via synthesis of NO is straightforward, we cannot rule out the possibility that the effect of Tacr1 neurons on blood flow may be indirect. For instance, Tacr1 neurons could exert an effect on astrocytes, which then would signal to blood vessels, or Tacr1 neurons could alter network activity, which would then alter blood supply. Consistent with this idea, previous studies have shown that optogenetic stimulation of Nos1 neurons evokes a small change in field potential.[22,67] Furthermore, while L-NPA demonstrates strong inhibition of nNOS,[68,69] some groups indicate a 4-fold selectivity for nNOS over endothelial NOS (eNOS) in human tissue,[70,71] and, therefore, it is possible that in our experiments, L-NPA might have inhibited both eNOS and nNOS. Another limitation in this study is that all human brain tissue samples were obtained from male subjects, thereby preventing our ability to identify any potential sex differences in Tacr1 neuron expression in humans. Finally, we acknowledge that we focused our study on the whisker somatosensory cortex and that it did not encompass the entire cortical vascular tree, limiting our analysis of vascular dynamics. Also, we did not systemically investigate other brain regions, such that the generalizability of our findings across the brain remains to be determined.

STAR★METHODS

RESOURCE AVAILABILITY

Lead contact—Further information and requests for resources and reagents should be directed to and will be fulfilled by the lead contact, Alberto Vazquez (alv15@pitt.edu).

Materials availability—All materials used in this study are commercially available.

Data and code availability

- All data that support the findings of this study are available from the lead contact upon request. Processed calcium imaging mouse data and optogenetic mouse

data have been deposited at GitHub and are publicly available. The DOI is listed in the key resources table.

- Costume code used for analyzing calcium imaging and optogenetic data have been deposited at GitHub and are publicly available as of the date of publication. The DOI is listed in the key resources table.
- Any additional information required to reanalyze the data reported in this paper is available from the lead contact upon request.

EXPERIMENTAL MODEL AND SUBJECT DETAILS

Mice—All animals were cared for in compliance with the National Institutes of Health guidelines and approved by the University of Pittsburgh Institutional Animal Care and Use Committee. Mice were given free access to food and water and housed under standard laboratory conditions and were kept on a 12 h light/dark cycle. Previously generated[35] *Tacr1*^{CreER} mice (also called *NK1R*^{CreER} mice) were bred in house and maintained on a C57BL/6 background. The following mice strains were used: wild type (C57BL/6J, Charles River, no. 027), *NG2*^{CreER} (Hartmann et al.[51]; JAX, no. 008538), Ai9 (JAX, no. 007909), Ai32 (JAX, no. 012569), Ai35 (Madisen et al.[76]; JAX, no. 012735), Ai95 (JAX, no. 028865), Thy1-GCaMP6s (JAX, no. 024275). All mice were maintained on a C57BL/6J background, and both males and females were used. In all cases, no differences between male and female mice were observed and so the data was pooled. For circuit mapping experiments, coronal brain slabs were used from mice ranging from 42 to 92 days of age. For all other experiments, adult, ranging from 8 to 16 weeks of age, were used. For mice expressing CreER, tamoxifen (Sigma-Aldrich, T5648) was dissolved in corn oil at a concentration of 20 mg mL^{-1} and injected into peritoneal cavities at a dose 100 mg kg^{-1} for 5 consecutive days. Animals recovered for at least one week following the last tamoxifen treatment before cranial surgery or dissections were performed. Sample sizes were determined by a power calculation based on previous pilot data and representative sample sizes from previous literature that had similar experiments.

Human samples—Human brain tissue was obtained from the University of Pittsburgh NIH NeuroBioBank Brain and Tissue Repository in compliance with the University of Pittsburgh's Committee for Oversight of Research and Clinical Training involving Decedents and the Institutional Review Board for Biomedical Research. Brain tissue from the prefrontal cortex was collected from adult human organ donors (donor 1: white, 39-year-old male, donor 2: white, 42-year-old male, and donor 3: white, 46-year-old male), flash frozen, and stored at 80°C until use. Procedures involving human tissue were approved by the Institutional Review Board for Biomedical Research and The University of Pittsburgh's Committee for the Oversight of Research and Clinical Training Involving Decedents.

METHOD DETAILS

Immunohistochemistry—Tamoxifen-treated *Tacr1*^{CreER}; *Rosa26*$^{lsl\text{-}tdT}$(Ai9) adult mice were transcardially perfused with 4% paraformaldehyde (PFA). Brains were dissected out of the skull and post-fixed overnight. Sagittal or transverse 40 μm sections were cut on a vibratome (Leica 1200) and processed for free-floating IHC. Brain sections were

blocked with 10% goat or donkey serum, phosphate-buffered saline + Triton (0.1% Triton X-100, PBST) and stained overnight at 4°C with the following primary antibodies at the indicated concentrations: GFP (1:1000; ThermoFisher A-11122; Aves Lab Inc., GFP-1020), Tacr1 (1:10,000; Sigma S8305), nNOS (1:2000, Abcam Ab1376), neuropeptide Y (1:1000; Peninsula Laboratories, LLC; T-4070), parvalbumin (1:2000; SWANT; PVG-213), RFP (1:1000; Rockland; 600–401-379S) and somatostatin (1:1000; Peninsula Laboratories, LLC; T-4547), followed by the corresponding Alexa Fluor-conjugated secondary antibodies (1:500, ThermoFisher). Sections were mounted in Fluoromount-G (SouthernBiotech) and imaged with confocal microscopy (Nikon A1R) and fluorescent microscopy (Nikon 90i). Anatomical regions were identified using the Paxinos and Allen Institute Mouse Brain Atlases.

Transmission electron microscopy—Adult *Tacr1*^{CreER}; *Rosa26*$^{lsl\text{-}ChR2\text{-}eYPF}$ mice were anesthetized and then transcardially perfused with 0.1M phosphate buffer (PB) pH = 7.2, followed by 4% PFA and 0.5% glutaraldehyde in 0.1 M phosphate buffer (PB). Brains were post-fixed for 90 min in the same fixative at 4°C. Following fixation, 80 μm coronal sections were cut by vibratome in 0.1M PB and then cryoprotected with an ascendant gradient of glycerol in 0.1M PB. The glycerol gradient involved two 30-min incubations (10% and 20%), followed by an overnight incubation in 30% glycerol. Sections were frozen on dry ice and thawed in 0.1M PB. For the IHC, sections were blocked with 10% normal goat serum for 1 h at room temperature (RT), incubated overnight at 4°C with a rabbit anti-GFP primary antibody (1:1000; ThermoFisher A-11122) in 0.1M PB, and were followed by 2 h incubation at RT in a biotinylated secondary antibody goat anti-rabbit (1:1000; Jackson Laboratories) in 0.1M PB. After, sections were incubated in avidin biotin peroxidase complex (ABC Elite; Vector Laboratories; 60 min; RT), washed in 0.1M PB and developed with 3, 3-diaminobenzidine plus nickel (DAB; Vector Laboratories Kit; 2–5 min reaction). Sections were washed in 0.1M cacodylate buffer and postfixed with 1% osmium and 1.5% potassium ferrocyanide in cacodylate buffer for 1 h at RT after sections were dehydrated in an ascending gradient of ethanol (ETOH; 35%, 50% 70%, 85% 90%). Sections were blocked-stained with 3% uranyl acetate in 70% ETOH for 2 h at 4°C before the 80% ETOH. Latest steps of dehydration were performed with 100% ETOH, propylene oxide followed by infiltration with epoxy resin (EMBed-812; Electron Microscopy Science, PA USA). Sections were flatted embedded between Aclar sheets and polymerized in an oven at 60°C for 48 h. Selected areas of the cortex were trimmed and mounted on epoxy blocks and cut with a Leica EM UC7 ultramicrotome. Ultrathin sections (80 nm in thickness) were collected on single slot cupper grids with formvar. Ultrathin sections were observed with a JEOL-1400 transmission electron microscope (JEOL Ltd., Akishima Tokyo, Japan) and images were captured with an Orius SC200 CCD camera (Gatan Inc., Warrendale, PA, USA).

Multiplex fluorescence *in situ* hybridization (FISH)—Mice were anesthetized with 3–5% isoflurane and rapidly decapitated. The brain was quickly removed (<2 min), placed into OCT, and flash frozen using 2-methylbutane chilled on dry ice. Tissue was kept on dry ice until cryosectioning. Cryosections (15 μm) were mounted directly onto Super Frost Plus slides, and FISH studies were performed according to the protocol for fresh-frozen

sample using the RNAscope Multiplex Fluorescent v1 Assay (Advanced Cell Diagnostics, ACD, 320850). Probes (Advanced Cell Diagnostics) for Mm-Tacr1 (Cat. No. 428781), Mm-tdTomato (Cat. No. 317041) Mm-Nos1 (Cat. No. 437651), Mm-Chodl (Cat. No. 450211) and Mm-Sst (Cat. No. 404631) were hybridized for 2 h at 40°C in a humidified oven, followed by rinsing in wash buffer and a series of incubations to develop the hybridized probe signal. Human prefrontal cortex was cryosectioned at 20 μm and mounted directly onto Super Frost Plus slides and FISH studies were performed according to the protocol for fresh-frozen sample using the RNAscope Multiplex Fluorescent v2 Assay (ACD, 320850). Human probes included Hu-TACR1 (Cat. No.17166A), Hu-NOS1 (Cat. No. 171594), Hu-CHODL (Cat. No.171634) and Hu-SST (Cat. No. 17145C). Sections were stained with DAPI (320858) and mounted with Prolong Diamond AntiFade (ThermoFisher, P36961).

Image acquisition and quantification—Sections were imaged using either a confocal microscope (Nikon A1R) or a fluorescent microscope (Nikon 90i). All IHC images were quantified and analyzed using the cell counter tool in ImageJ.[37] To quantify images in FISH experiments, confocal images of tissue samples were imaged and only cells whose nuclei were clearly visible by DAPI staining and exhibited fluorescent signal were counted.

Stereotaxic injection and viruses—Animals were anesthetized with 3–5% isoflurane and maintained at 1–2% isoflurane for the duration of the procedure. Animals were placed in a stereotaxic head frame (Kopf Instruments, Model 942 Small Animal Stereotaxic Instruments) and administered a subcutaneous dose of the analgesic (buprenorphine, 0.1 mg kg^{-1}; ketoprofen, 5.0 mg kg^{-1}) at the start of the procedure and was also administered ketoprofen BID for 48 h after the procedure. The scalp was shaved, local antiseptic applied (betadine), and a midline incision made to expose the cranium. The skull was aligned using cranial fissures. Local anesthetic bupivacaine (2.5 mg kg^{-1}) was topically applied on the skull at the site of drilling. A stainless-steel burr (Fine Science Tools, 19008–07) attached to a micro drill (Foredom Electric Co., K1070 High Speed Rotary Micromotor Kit, 2.35mm Collet) was used to create a burr hole. A custom pulled 3.5″ glass capillary tube (Drummond Scientific Company, #3–00-203-G/X replacement) was loaded with AAV. Virus was infused at a rate of 2 nL/s using a microinjector (Drummond Scientific Company, Nanoinjector III, Cat.#3–000-207). *Tacr1*^{CreER} mice were unilaterally injected with 400 nL virus. The injection needle was left in place for an additional 5 min and then slowly withdrawn. Injections performed at the following coordinates for each brain region: S1BF: AP, −0.60 mm; ML, ±2.9 mm; DV: 0.5 and 0.8 mm. The skin incision was closed using 2–3 simple interrupted sutures. A small amount (<5 μL) of 3M Vetbond was placed on top of sutures to discourage grooming-related activities at the incision site. Mice were housed with original cage-mates and given 4 weeks to recover prior to experimentation.

The following viruses were used in this study: AAVr.EF1a.DIO.hChR2(H134R).EYFP-WPRE-HGH (Addgene 20298), AAV5-hSyn-Con/Foff-hChR2(h134R)-EYFP (Addgene 55646)[72] and AAV9-CaMKIIa-hChR2(H134R)-EYFP (Addgene 26969).[73]

Whole tissue clearing—Whole-tissue clearing on *Tacr1*^{CreER} mouse brains injected with AAVrg-DIO-ChR2-YFP (Addgene 20298) was performed using the CUBIC (unobstructed brain/body imaging cocktails) protocol.[74] Animals were transcardially perfused with 1x

PBS and then 4% PFA. The perfused brains were post-fixed overnight in 4% PFA at 4°C. Brains were incubated in 50% CUBIC R1 solution at 37°C on a nutating shaker until brains were translucent. Brains were then washed with IHC buffer and incubated in primary antibody (GFP, 1:500 ThermoFisher A-11122), followed with the corresponding Alexa Fluor-conjugated secondary antibodies (1:500, ThermoFisher). Antibody incubations were completed for 1 week. Brains were refractive index matched using CUBIC R2 solution at 37°C on a nutating shaker until clear. Ribbon scanning microscopy of whole cortex was completed on an RS-G4 confocal microscope (Caliber ID, Andover, MD) fitted with a Nikon CFI90 20x, 1.00 NA, glycerol objective. Data were acquired at a resolution of ~0.3 μm lateral and ~10 μm axial. The imaged data was stitched and assembled using a 24-node compute cluster running custom software. Neurons were traced using the filaments tool in Imaris v9.7.2 (Bitplane) software first using the semi-automated Autopath tool then corrected using the manual editing tools.

Circuit mapping—For subcellular ChR2-assisted circuit mapping (sCRACM) experiments, TTX (1 μm, Tocris Bioscience), and 4-AP (100 μm, Sigma) were added to the oxygenated ACSF (in mm: 127 NaCl, 25 NaHCO3, 25 d-glucose, 2.5 KCl, 2 CaCl2, 1 MgCl2, 1.25 NaH2PO4) containing potassium gluconate-based internal solution (in mm: 128 potassium gluconate, 4 MgCl2, 10 HEPES, 1 EGTA, 4 Na2ATP, 0.4 Na2GTP, 10 sodium phosphocreatine, 3 sodium l-ascorbate; pH 7.27; 287 mOsm).[75] Afterward, whole-cell recordings from M1 neurons were performed in coronal brain slices of mice aged P42–92 with thalamic or S1 axons expressing ChR2 and applied 1 ms flashes of blue light (~1 mW) to evoke neurotransmitter release. To prevent polysynaptic activity, we further added TTX (1 mM) and 4-AP (100 mM). Data were acquired at 10 kHz using an Axopatch 700B (Molecular Devices) and Ephus software on a custom-built laser scanning photostimulation microscope. The recordings were done in M1 as no sensory-evoked (whisker stimulation) changes were part of the experimental design. The data from sCRACM can be generalized to all cortical Tacr1 neurons. Individual maps were repeated 2–4 times and averaged. Electrophysiology data were low pass filtered offline (1 kHz). This method enables ChR2-expressing axons near the laser to locally release glutamate upon photostimulation. Data analysis was performed with custom routines written in MATLAB (MathWorks).

Chronic cranial windows and cannula implantation—Two-to four-month-old mice underwent a craniotomy involving implantation of a sterile glass window and attachment of an aluminum chamber frame (Narishige Inc., CF-10). Mice were anesthetized with 3–5% isoflurane and maintained at 1–2% isoflurane for the duration of the procedure. The respiration rate and body temperature were continuously monitored throughout the procedure to ensure the appropriate level of anesthesia. A subcutaneous dose of analgesia, buprenorphine (0.1 mg kg^{-1}) and ketoprofen (5.0 mg kg^{-1}), was administered at the start of the procedure and twice a day for three additional days after the craniotomy. A local anesthetic (bupivacaine, 2.5 mg kg^{-1}) was topically applied on skull at the site of the craniotomy. The craniotomy was centered over barrel cortex, approximately 1.5–2 mm posterior to bregma and 3 mm lateral to the midpoint between bregma and lambda. A custom cover glass consisting of a 4-mm round cover glass glued onto a 5-mm round cover glass (CS-4R and CS-5R, Warner Instruments Inc.), and a chamber frame were cemented

with dental cement (Lang Dental Manufacturing Company, Ortho-Jet) onto the skull. Tamoxifen administration (100 mg kg^{-1}) in *Tacr1*^{CreER} mice began 3 days post-surgery. During recovery, the mice were acclimated to a custom treadmill with a head holder plate (Narishige Inc., MAG-1) for awake head-fixed data collection. For the cannula implantation, a small indentation (<0.5mm) right next to the cranial window craniotomy was made to insert the cannula (RWD Life Science Inc., Guide Cannula-Single 3 mm length and Injector-Single). The cannula was cemented using dental acrylic (Stoelting Co., Wood Dale, IL) and cyanoacrylate glue (3M Vetbond Tissue Adhesive). The cannula was positioned in a 30° angle near the barrel cortex and inserted about100 μm beneath the cortical surface while avoiding large surface vessels.

Intracortical infusions—Animals were head-fixed on the custom treadmill while the dummy cannula was gently removed following the baseline experiment. Afterward, the infusion cannula was inserted into the guide cannula. The infusions were done at a rate of 0.2 μL/min for 5 min for a total of 1μL using a programmable syringe pump (New Era Pump Systems Inc., Farmingdale, NY). Following the intracortical infusions, the mice remained head-fixed, and the whisker stimulation experiments began while keeping the infusion cannulas connected for the remaining of the experiment. For pharmacological experiments, we dissolved N ω-propyl-L-arginine (L-NPA) with sterile 1x PBS to make a final concentration of 1 mM. For vehicle experiments, we used sterile 1x PBS.

Optogenetic stimulation—Light and whisker stimulation experiments were performed in animals under awake head-fixed conditions. The light stimulus was delivered using a power-adjustable, TTL-controlled laser diode unit (CrystaLaser Inc., Reno, NV) connected to the optic fiber. The laser power at the tip of the fiber was set to 1 mW using a power meter (Melles Griot 13p.m.001, IDEX Inc., Rochester, NY). Air puffs were delivered using a pressure injector (Toohey Spritzer, Toohey Company, Fairfield, NJ) set to 30 psi. The light stimulation parameters were selected based on previous experiments.[17,39] For activation of Channelrhodopsin, a 473-nm laser delivered 30 ms light pulse at 5 Hz for 1 s every 30 s. For activation archaerhodopsin (ArchT), 589-nm laser delivered 5 ms light pulses at 5 Hz for 1 s every 30 s. At least 10 stimulation trials were collected for each stimulation parameter set. For optogenetic silencing experiments, whisker stimulation was performed before ($whisker_{initial}$) and after ($whisker_{final}$) light inhibition. Additional experiments were conducted in a subset of mice to serve as control experiments. Control experiments were performed in either *Tacr1*^{CreER} mice (ChR2 negative) or *Tacr1*^{CreER} mice expressing eYFP or GCaMP6f rather than ChR2. Stimulation triggers and LDF data were recorded at 1 kHz (MP150, Biopac Systems Inc., Goleta, CA).

Laser Doppler flowmetry—A laser Doppler flowmeter (LDF; Periflux 5000/411, Perimed AB, Jarfalla, Sweden) was used to acquire CBF data in response to optogenetic (light) or whisker stimulation (air puff). The LDF probe used has a tip diameter of 200 mm, operating wavelength of 780 nm and a sampling rate of 1 kHz. Time series spanning 30 s were obtained from all trials starting 5 s prior to stimulation onset. The LDF time series were low-pass filtered with a rectangular cut-off of 4Hz and down-sampled to 10 Hz. An air puffer was also placed in front of the contralateral whisker pad (50 ms puffs, delivered at 5

Hz). LDF was used to measure changes in CBF. We also sampled the backscatter reading from the LDF unit and used to regress out optogenetic stimulation artifacts in LDF traces (during the stimulation period) for stimulation frequencies of 5 and 10Hz. The change in CBF (DCBF) was calculated as (CBF_{time}-$CBF_{baseline}$)/$CBF_{baseline}$ x 100. $CBF_{baseline}$ was determined as the mean CBF during the 4 s before whisker or light stimulation. Time series from all trials (10–12 trials) were averaged and converted to percent change for each animal and then averaged across animals. The change in maximum CBF (Max. ΔCBF) was determined as the average value during 1–3 s after whisker or light stimulation. Maximum CBF (%) difference was determined as the max. ΔCBF light ON – max. ΔCBF light OFF (ChR2) or ΔCBF light OFF – max. DCBF light ON (ArchT).

Two-photon microscopy—*In vivo* 2P microscopy cortical imaging was performed using an Ultima IV microscope (Bruker Nano Analytics) coupled to an ultra-fast laser (Excite X3, Newport Spectra-Physics, Inc). Awake, head-fixed mice were placed on a custom-made setup designed to accommodate light and sensory stimulation during live brain imaging. 2P images were acquired using a 16×water immersion objective lens (0.80 NA, Nikon, Inc.) at a wavelength of 920 nm for studies imaging YFP/GFP, GCaMP6f and vasculature. Images were obtained with a maximum field-of-view of 800 × 800 μm. We calibrate the laser power output through the objective lens and use <40 mW for time series imaging. Stimulus onset (t = 0) and imaging recordings were synchronized using a National Instruments board that tracked the start-of-frame trigger. All time series images were motion corrected using a Fourier based, translation-only algorithm implemented in MATLAB. The first frame in each time series was used as a refence.

QUANTIFICATION AND STATISTICAL ANALYSIS

Vessel analysis—A subcutaneous injection of SR 101 (Thermo Fisher Scientific, 0.2 μL g^{-1}) was administered in mice to visualize the cerebral vasculature *in vivo*. We imaged parenchymal arterioles and capillary branches from the middle cerebral artery. We identified a pial artery in the somatosensory cortex and traced its branching parenchymal arterioles and capillaries (cortex depth, approximately 0–500 μm). To distinguish arterioles and capillaries *in vivo*, selection of arterioles and capillaries were guided by eYFP labeling of VSMCs (NG2-GCaMP6f). Ten stimulation trials were acquired and averaged for each field of view. Three to seven locations were acquired per imaging session. Multiple imaging sessions were collected on separate days per mouse and arteriolar and capillary dilation responses were averaged across all sessions for each mouse. To determine percent change in diameter relative to baseline, the time series images were first filtered with a Gaussian filter and background subtracted with a rolling ball of 50 pixels. The diameter was measured as the full-width half-max of the vessel profile using custom MATLAB routines. Time series were then smoothed using the default smooth function in MATLAB (moving average or Savitzky-Golay smoother, 5 points). The change in vessel diameter (ΔD/D) was determined as ($diameter_{time}$ - $diameter_{baseline}$)/$diameter_{baseline}$. $Diameter_{baseline}$ was determined as the mean diameter during the 4 s before whisker or light stimulation. The maximum vessel dilation was determined as the maximum value before (t < −1 s) or after (t > 1.5 s) whisker or light stimulation (t = time). To determine latency onset to dilate, a line was fitted through 20% and 80% of the maximum value. The latency onset to dilate was considered

the time difference between the x-intercept of the line and the start of the whisker or light stimulation.

Calcium (Ca^{2+}) imaging—For determination of calcium responses in GCaMP6f labeled neurons in *Tacr1*^{CreER}-GCaMP6f mice, or VSMCs in *NG2*^{CreER}: GCaMP6f mice, a region of interest (ROI) was selected encompassing individual cells or VSMCS. Ca^{2+} transients in regions of interested were longitudinally recorded by 2P microscopy (excitation: 920 nm). Cell morphology, distinguishable by YFP labeling, was used to unambiguously identify pericytes (vs. VSMC or oligodendrocytes) *in vivo*. In addition, VSMC identity was confirmed post hoc from Z-stacks of imaging sessions based on a combination of branching order, vessel diameter, and distance from the parenchymal arteriole.[32,53] Ca^{2+} responses were quantified with MATLAB. Briefly, the change in the Ca^{2+} signal (ΔF/F) was calculated as ($fluorescence_{time}$-$fluorescence_{baseline}$)/$fluorescence_{baseline}$. $Fluorescence_{baseline}$ intensity was determined as the average intensity for all time points for spontaneous activity measurements. For VSMCs, the minimum Ca^{2+} signal response was determined as the minimum value after (t > 1.5 s) whisker or light stimulation. To determine latency onset to relaxation, a line was fitted through 20% and 80% of the maximum value. The latency onset to relaxation was considered the time difference between the x-intercept of the line and the start of the whisker or light stimulation. For neurons, the maximum calcium response was determined as the maximum value after (t > 1.5 s) whisker or light stimulation. Time series were smoothed using the smooth function in MATLAB (Savitzky-Golay or moving average smoother, 5 points, adapted for multiple vectors).

Statistical analyses—All statistical analyses were performed using Prism 9 (GraphPad Software). Two group comparisons were analyzed using a two-tailed paired *t* test (Figures 2J, 2N, 2R, 3E, 3F, and 6H), paired non-parametric (Figure 2C), and unpaired non-parametric (Figures 2K, 2O, 3G, 3H, S5G, and S5N) analyses. Multiple group comparisons were analyzed using a one-way ANOVA, followed by a post hoc Bonferroni analysis to correct for multiple comparisons (Figures S5C, S5F, S5J, S5M, and S6C). No data were excluded when performing statistical analysis. No methods were used to test if the data met the assumptions of the statistical approach. The s.e.m. was calculated for all experiments and displayed as errors bars in graphs. Statistical details for specific experiments (e.g., exact n values and what n represents, precision measures, statistical tests used and definitions of significance) can be found in figure legends. Values are expressed as mean ± s.e.m. No animals were excluded from analyses.

Supplementary Material

Refer to Web version on PubMed Central for supplementary material.

ACKNOWLEDGMENTS

We thank the donors and their loved ones for making our human studies possible and the Brain Tissue Donation Program at the University of Pittsburgh and the NIH NeuroBioBank for providing human prefrontal cortical sections. The University of Pittsburgh's Committee for the Oversight of Research and Clinical Training Involving Decedents and Institutional Review Board for Biomedical Research approved all procedures. This work was funded in part by NIH grants F31-NS106724 to C.F.R., F31-NS132422 to F.J.A., F30-MH124329 to S.J.D., R01-NS090444 and R01-NS117515 to A.L.V., R01-NS119410 to S.E.R., R01-NS103993 to B.M.H., R01-DC013048

to M.E.R., and R01-MH119701 to K.N.F., as well as by the Alzheimer's Disease Research Center (ADRC) of the University of Pittsburgh.

REFERENCES

1. Attwell D, Buchan AM, Charpak S, Lauritzen M, Macvicar BA, and Newman EA (2010). Glial and neuronal control of brain blood flow. Nature 468, 232–243. 10.1038/nature09613. [PubMed: 21068832]
2. Iadecola C. (2017). The Neurovascular Unit Coming of Age: A Journey through Neurovascular Coupling in Health and Disease. Neuron 96, 17–42. 10.1016/j.neuron.2017.07.030. [PubMed: 28957666]
3. Yu X, Ji C, and Shao A. (2020). Neurovascular Unit Dysfunction and Neurodegenerative Disorders. Front. Neurosci 14, 334. 10.3389/fnins.2020.00334. [PubMed: 32410936]
4. Iadecola C. (2004). Neurovascular regulation in the normal brain and in Alzheimer's disease. Nat. Rev. Neurosci 5, 347–360. 10.1038/nrn1387. [PubMed: 15100718]
5. Iadecola C. (2013). The pathobiology of vascular dementia. Neuron 80, 844–866. 10.1016/j.neuron.2013.10.008. [PubMed: 24267647]
6. Mattsson N, Tosun D, Insel PS, Simonson A, Jack CR Jr., Beckett LA, Donohue M, Jagust W, Schuff N, and Weiner MW; Alzheimer's Disease Neuroimaging Initiative (2014). Association of brain amyloid-beta with cerebral perfusion and structure in Alzheimer's disease and mild cognitive impairment. Brain 137, 1550–1561. 10.1093/brain/awu043. [PubMed: 24625697]
7. Thal DR, Grinberg LT, and Attems J. (2012). Vascular dementia: different forms of vessel disorders contribute to the development of dementia in the elderly brain. Exp. Gerontol 47, 816–824. 10.1016/j.exger.2012.05.023. [PubMed: 22705146]
8. Schaeffer S, and Iadecola C. (2021). Revisiting the neurovascular unit. Nat. Neurosci 24, 1198–1209. 10.1038/s41593-021-00904-7. [PubMed: 34354283]
9. O'Gallagher K, Rosentreter RE, Elaine Soriano J, Roomi A, Saleem S, Lam T, Roy R, Gordon GR, Raj SR, Chowienczyk PJ, et al. (2022). The Effect of a Neuronal Nitric Oxide Synthase Inhibitor on Neurovascular Regulation in Humans. Circ. Res 131, 952–961. 10.1161/CIRCRESAHA.122.321631. [PubMed: 36349758]
10. Cauli B, Tong XK, Rancillac A, Serluca N, Lambolez B, Rossier J, and Hamel E. (2004). Cortical GABA interneurons in neurovascular coupling: relays for subcortical vasoactive pathways. J. Neurosci 24, 8940–8949. 10.1523/JNEUROSCI.3065-04.2004. [PubMed: 15483113]
11. Echagarruga CT, Gheres KW, Norwood JN, and Drew PJ (2020). nNOS-expressing interneurons control basal and behaviorally evoked arterial dilation in somatosensory cortex of mice. Elife 9, e60533. 10.7554/eLife.60533.
12. Hoiland RL, Caldwell HG, Howe CA, Nowak-Flu€ck D, Stacey BS, Bailey DM, Paton JFR, Green DJ, Sekhon MS, Macleod DB, and Ainslie PN (2020). Nitric oxide is fundamental to neurovascular coupling in humans. J. Physiol 598, 4927–4939. 10.1113/JP280162. [PubMed: 32785972]
13. Iadecola C. (1993). Regulation of the cerebral microcirculation during neural activity: is nitric oxide the missing link? Trends Neurosci. 16, 206–214. 10.1016/0166-2236(93)90156-g. [PubMed: 7688160]
14. Lourenc o, C.F., Ledo A, Barbosa RM, and Laranjinha J. (2017). Neurovascular-neuroenergetic coupling axis in the brain: master regulation by nitric oxide and consequences in aging and neurodegeneration. Free Radic. Biol. Med 108, 668–682. 10.1016/j.freerad-biomed.2017.04.026. [PubMed: 28435052]
15. Paul A, Crow M, Raudales R, He M, Gillis J, and Huang ZJ (2017). Transcriptional Architecture of Synaptic Communication Delineates GABAergic Neuron Identity. Cell 171, 522–539.e20. 10.1016/j.cell.2017.08.032. [PubMed: 28942923]
16. Tasic B, Menon V, Nguyen TN, Kim TK, Jarsky T, Yao Z, Levi B, Gray LT, Sorensen SA, Dolbeare T, et al. (2016). Adult mouse cortical cell taxonomy revealed by single cell transcriptomics. Nat. Neurosci 19, 335–346. 10.1038/nn.4216. [PubMed: 26727548]

17. Vazquez AL, Fukuda M, and Kim SG (2018). Inhibitory Neuron Activity Contributions to Hemodynamic Responses and Metabolic Load Examined Using an Inhibitory Optogenetic Mouse Model. Cereb. Cortex 28, 4105–4119. 10.1093/cercor/bhy225. [PubMed: 30215693]

18. Dittrich L, Heiss JE, Warrier DR, Perez XA, Quik M, and Kilduff TS (2012). Cortical nNOS neurons co-express the NK1 receptor and are depolarized by Substance P in multiple mammalian species. Front. Neural Circuits 6, 31. 10.3389/fncir.2012.00031. [PubMed: 22679419]

19. Perrenoud Q, Geoffroy H, Gauthier B, Rancillac A, Alfonsi F, Kessaris N, Rossier J, Vitalis T, and Gallopin T. (2012). Characterization of Type I and Type II nNOS-Expressing Interneurons in the Barrel Cortex of Mouse. Front. Neural Circuits 6, 36. 10.3389/fncir.2012.00036. [PubMed: 22754499]

20. Ahn SJ, Anfray A, Anrather J, and Iadecola C. (2023). Calcium transients in nNOS neurons underlie distinct phases of the neurovascular response to barrel cortex activation in awake mice. J. Cereb. Blood Flow Metab 43, 1633–1647. 10.1177/0271678X231173175. [PubMed: 37149758]

21. Krawchuk MB, Ruff CF, Yang X, Ross SE, and Vazquez AL (2020). Optogenetic assessment of VIP, PV, SOM and NOS inhibitory neuron activity and cerebral blood flow regulation in mouse somato-sensory cortex. J. Cereb. Blood Flow Metab 40, 1427–1440. 10.1177/0271678X19870105. [PubMed: 31418628]

22. Lee L, Boorman L, Glendenning E, Christmas C, Sharp P, Redgrave P, Shabir O, Bracci E, Berwick J, and Howarth C. (2020). Key Aspects of Neurovascular Control Mediated by Specific Populations of Inhibitory Cortical Interneurons. Cereb. Cortex 30, 2452–2464. 10.1093/cercor/bhz251. [PubMed: 31746324]

23. Vo TT, Im GH, Han K, Suh M, Drew PJ, and Kim SG (2023). Parvalbumin interneuron activity drives fast inhibition-induced vasoconstriction followed by slow substance P-mediated vasodilation. Proc. Natl. Acad. Sci. USA 120, e2220777120. 10.1073/pnas.2220777120.

24. He M, Tucciarone J, Lee S, Nigro MJ, Kim Y, Levine JM, Kelly SM, Krugikov I, Wu P, Chen Y, et al. (2016). Strategies and Tools for Combinatorial Targeting of GABAergic Neurons in Mouse Cerebral Cortex. Neuron 91, 1228–1243. 10.1016/j.neuron.2016.08.021. [PubMed: 27618674]

25. Hosford PS, and Gourine AV (2019). What is the key mediator of the neurovascular coupling response? Neurosci. Biobehav. Rev 96, 174–181. 10.1016/j.neubiorev.2018.11.011. [PubMed: 30481531]

26. Fernández-Klett F, Offenhauser N, Dirnagl U, Priller J, and Lindauer U. (2010). Pericytes in capillaries are contractile in vivo, but arterioles mediate functional hyperemia in the mouse brain. Proc. Natl. Acad. Sci. USA 107, 22290–22295. 10.1073/pnas.1011321108. [PubMed: 21135230]

27. Hill RA, Tong L, Yuan P, Murikinati S, Gupta S, and Grutzendler J. (2015). Regional Blood Flow in the Normal and Ischemic Brain Is Controlled by Arteriolar Smooth Muscle Cell Contractility and Not by Capillary Pericytes. Neuron 87, 95–110. 10.1016/j.neuron.2015.06.001. [PubMed: 26119027]

28. Vanlandewijck M, He L, Mä e MA, Andrae J, Ando K, Del Gaudio F, Nahar K, Lebouvier T, Laviña B, Gouveia L, et al. (2018). A molecular atlas of cell types and zonation in the brain vasculature. Nature 554, 475–480. 10.1038/nature25739. [PubMed: 29443965]

29. Alarcon-Martinez L, Villafranca-Baughman D, Quintero H, Kacerovsky JB, Dotigny F, Murai KK, Prat A, Drapeau P, and Di Polo A. (2020). Interpericyte tunnelling nanotubes regulate neurovascular coupling. Nature 585, 91–95. 10.1038/s41586-020-2589-x. [PubMed: 32788726]

30. Cai C, Fordsmann JC, Jensen SH, Gesslein B, Lønstrup M, Hald BO, Zambach SA, Brodin B, and Lauritzen MJ (2018). Stimulation-induced increases in cerebral blood flow and local capillary vasoconstriction depend on conducted vascular responses. Proc. Natl. Acad. Sci. USA 115, E5796–E5804. 10.1073/pnas.1707702115.

31. Gonzales AL, Klug NR, Moshkforoush A, Lee JC, Lee FK, Shui B, Tsoukias NM, Kotlikoff MI, Hill-Eubanks D, and Nelson MT (2020). Contractile pericytes determine the direction of blood flow at capillary junctions. Proc. Natl. Acad. Sci. USA 117, 27022–27033. 10.1073/pnas.1922755117.

32. Grant RI, Hartmann DA, Underly RG, Berthiaume AA, Bhat NR, and Shih AY (2019). Organizational hierarchy and structural diversity of microvascular pericytes in adult mouse cortex. J. Cereb. Blood Flow Metab 39, 411–425. 10.1177/0271678X17732229. [PubMed: 28933255]

33. Kisler K, Nelson AR, Rege SV, Ramanathan A, Wang Y, Ahuja A, Lazic D, Tsai PS, Zhao Z, Zhou Y, et al. (2017). Pericyte degeneration leads to neurovascular uncoupling and limits oxygen supply to brain. Nat. Neurosci 20, 406–416. 10.1038/nn.4489. [PubMed: 28135240]
34. Zambach SA, Cai C, Helms HCC, Hald BO, Dong Y, Fordsmann JC, Nielsen RM, Hu J, Lønstrup M, Brodin B, and Lauritzen MJ (2021). Precapillary sphincters and pericytes at first-order capillaries as key regulators for brain capillary perfusion. Proc. Natl. Acad. Sci. USA 118, e2023749118. 10.1073/pnas.2023749118.
35. Huang H, Kuzirian MS, Cai X, Snyder LM, Cohen J, Kaplan DH, and Ross SE (2016). Generation of a NK1R-CreER knockin mouse strain to study cells involved in Neurokinin 1 Receptor signaling. Genesis 54, 593–601. 10.1002/dvg.22985. [PubMed: 27712014]
36. Duchemin S, Boily M, Sadekova N, and Girouard H. (2012). The complex contribution of NOS interneurons in the physiology of cerebrovascular regulation. Front. Neural Circuits 6, 51. 10.3389/fncir.2012.00051. [PubMed: 22907993]
37. Schneider CA, Rasband WS, and Eliceiri KW (2012). NIH Image to ImageJ: 25 years of image analysis. Nat. Methods 9, 671–675. 10.1038/nmeth.2089. [PubMed: 22930834]
38. Tomioka R, Okamoto K, Furuta T, Fujiyama F, Iwasato T, Yanagawa Y, Obata K, Kaneko T, and Tamamaki N. (2005). Demonstration of long-range GABAergic connections distributed throughout the mouse neocortex. Eur. J. Neurosci 21, 1587–1600. 10.1111/j.1460-9568.2005.03989.x. [PubMed: 15845086]
39. Vazquez AL, Fukuda M, Crowley JC, and Kim SG (2014). Neural and hemodynamic responses elicited by forelimb- and photo-stimulation in channelrhodopsin-2 mice: insights into the hemodynamic point spread function. Cereb. Cortex 24, 2908–2919. 10.1093/cercor/bht147. [PubMed: 23761666]
40. Kitaura H, Uozumi N, Tohmi M, Yamazaki M, Sakimura K, Kudoh M, Shimizu T, and Shibuki K. (2007). Roles of nitric oxide as a vasodilator in neurovascular coupling of mouse somatosensory cortex. Neurosci. Res 59, 160–171. 10.1016/j.neures.2007.06.1469. [PubMed: 17655958]
41. Li J, Bravo DS, Upton AL, Gilmour G, Tricklebank MD, Fillenz M, Martin C, Lowry JP, Bannerman DM, and McHugh SB (2011). Close temporal coupling of neuronal activity and tissue oxygen responses in rodent whisker barrel cortex. Eur. J. Neurosci 34, 1983–1996. 10.1111/j.1460-9568.2011.07927.x. [PubMed: 22151136]
42. Matsuura T, and Kanno I. (2002). Effect of nitric oxide synthase inhibitor on the local cerebral blood flow evoked by rat somatosensory stimulation under hyperoxia. Comp. Biochem. Physiol. Mol. Integr. Physiol 131, 267–274. 10.1016/s1095-6433(01)00450-0.
43. Peng X, Zhang C, Alkayed NJ, Harder DR, and Koehler RC (2004). Dependency of cortical functional hyperemia to forepaw stimulation on epoxygenase and nitric oxide synthase activities in rats. J. Cereb. Blood Flow Metab 24, 509–517. 10.1097/00004647-200405000-00004. [PubMed: 15129182]
44. Lacroix A, Toussay X, Anenberg E, Lecrux C, Ferreirós N, Karagiannis A, Plaisier F, Chausson P, Jarlier F, Burgess SA, et al. (2015). COX-2-Derived Prostaglandin E2 Produced by Pyramidal Neurons Contributes to Neurovascular Coupling in the Rodent Cerebral Cortex. J. Neurosci 35, 11791–11810. 10.1523/JNEUROSCI.0651-15.2015. [PubMed: 26311764]
45. Williams RH, Vazquez-DeRose J, Thomas AM, Piquet J, Cauli B, and Kilduff TS (2018). Cortical nNOS/NK1 Receptor Neurons are Regulated by Cholinergic Projections From the Basal Forebrain. Cereb. Cortex 28, 1959–1979. 10.1093/cercor/bhx102. [PubMed: 28472227]
46. Vruwink M, Schmidt HH, Weinberg RJ, and Burette A. (2001). Substance P and nitric oxide signaling in cerebral cortex: anatomical evidence for reciprocal signaling between two classes of interneurons. J. Comp. Neurol 441, 288–301. 10.1002/cne.1413. [PubMed: 11745651]
47. Mancuso L, Costa T, Nani A, Manuello J, Liloia D, Gelmini G, Panero M, Duca S, and Cauda F. (2019). The homotopic connectivity of the functional brain: a meta-analytic approach. Sci. Rep 9, 3346. 10.1038/s41598-019-40188-3. [PubMed: 30833662]
48. Salvador R, Suckling J, Coleman MR, Pickard JD, Menon D, and Bullmore E. (2005). Neurophysiological architecture of functional magnetic resonance images of human brain. Cereb. Cortex 15, 1332–1342. 10.1093/cercor/bhi016. [PubMed: 15635061]

49. Stark DE, Margulies DS, Shehzad ZE, Reiss P, Kelly AMC, Uddin LQ, Gee DG, Roy AK, Banich MT, Castellanos FX, and Milham MP (2008). Regional variation in interhemispheric coordination of intrinsic hemodynamic fluctuations. J. Neurosci 28, 13754–13764. 10.1523/JNEUROSCI.4544-08.2008. [PubMed: 19091966]
50. Yan X, Kong R, Xue A, Yang Q, Orban C, An L, Holmes AJ, Qian X, Chen J, Zuo XN, et al. (2023). Homotopic local-global parcellation of the human cerebral cortex from resting-state functional connectivity. Neuroimage 273, 120010. 10.1016/j.neuroimage.2023.120010.
51. Hartmann DA, Underly RG, Grant RI, Watson AN, Lindner V, and Shih AY (2015). Pericyte structure and distribution in the cerebral cortex revealed by high-resolution imaging of transgenic mice. Neurophotonics 2, 041402. 10.1117/1.NPh.2.4.041402.
52. Hall CN, Reynell C, Gesslein B, Hamilton NB, Mishra A, Sutherland BA, O'Farrell FM, Buchan AM, Lauritzen M, and Attwell D. (2014). Capillary pericytes regulate cerebral blood flow in health and disease. Nature 508, 55–60. 10.1038/nature13165. [PubMed: 24670647]
53. Rungta RL, Chaigneau E, Osmanski BF, and Charpak S. (2018). Vascular Compartmentalization of Functional Hyperemia from the Synapse to the Pia. Neuron 99, 362–375.e4. 10.1016/j.neuron.2018.06.012. [PubMed: 29937277]
54. Rungta RL, Zuend M, Aydin AK, Martineau É, Boido D, Weber B, and Charpak S. (2021). Diversity of neurovascular coupling dynamics along vascular arbors in layer II/III somatosensory cortex. Commun. Biol 4, 855. 10.1038/s42003-021-02382-w. [PubMed: 34244604]
55. Boddum K, Jensen TP, Magloire V, Kristiansen U, Rusakov DA, Pavlov I, and Walker MC (2016). Astrocytic GABA transporter activity modulates excitatory neurotransmission. Nat. Commun 7, 13572. 10.1038/ncomms13572.
56. Haselden WD, Kedarasetti RT, and Drew PJ (2020). Spatial and temporal patterns of nitric oxide diffusion and degradation drive emergent cerebrovascular dynamics. PLoS Comput. Biol 16, e1008069. 10.1371/journal.pcbi.1008069.
57. Filosa JA, Morrison HW, Iddings JA, Du W, and Kim KJ (2016). Beyond neurovascular coupling, role of astrocytes in the regulation of vascular tone. Neuroscience 323, 96–109. 10.1016/j.neuroscience.2015.03.064. [PubMed: 25843438]
58. Perea G, Navarrete M, and Araque A. (2009). Tripartite synapses: astrocytes process and control synaptic information. Trends Neurosci. 32, 421–431. 10.1016/j.tins.2009.05.001. [PubMed: 19615761]
59. Uhlirova H, Kılıç K, Tian P, Thunemann M, Desjardins M, Saisan PA, Sakadžić S, Ness TV, Mateo C, Cheng Q, et al. (2016). Cell type specificity of neurovascular coupling in cerebral cortex. Elife 5, e14315. 10.7554/eLife.14315.
60. Gerashchenko D, Wisor JP, Burns D, Reh RK, Shiromani PJ, Sakurai T, de la Iglesia HO, and Kilduff TS (2008). Identification of a population of sleep-active cerebral cortex neurons. Proc. Natl. Acad. Sci. USA 105, 10227–10232. 10.1073/pnas.0803125105.
61. Kilduff TS, Cauli B, and Gerashchenko D. (2011). Activation of cortical interneurons during sleep: an anatomical link to homeostatic sleep regulation? Trends Neurosci. 34, 10–19. 10.1016/j.tins.2010.09.005. [PubMed: 21030095]
62. Morairty SR, Dittrich L, Pasumarthi RK, Valladao D, Heiss JE, Gerashchenko D, and Kilduff TS (2013). A role for cortical nNOS/NK1 neurons in coupling homeostatic sleep drive to EEG slow wave activity. Proc. Natl. Acad. Sci. USA 110, 20272–20277. 10.1073/pnas.1314762110.
63. Williams RH, Black SW, Thomas AM, Piquet J, Cauli B, and Kilduff TS (2019). Excitation of Cortical nNOS/NK1R Neurons by Hypocretin 1 is Independent of Sleep Homeostasis. Cereb. Cortex 29, 1090–1108. 10.1093/cercor/bhy015. [PubMed: 29462275]
64. Bergel A, Deffieux T, Demené C, Tanter M, and Cohen I. (2018). Local hippocampal fast gamma rhythms precede brain-wide hyperemic patterns during spontaneous rodent REM sleep. Nat. Commun 9, 5364. 10.1038/s41467-018-07752-3. [PubMed: 30560939]
65. Bojarskaite L, Vallet A, Bjørnstad DM, Gullestad Binder KM, Cunen C, Heuser K, Kuchta M, Mardal KA, and Enger R. (2023). Sleep cycle-dependent vascular dynamics in male mice and the predicted effects on perivascular cerebrospinal fluid flow and solute transport. Nat. Commun 14, 953. 10.1038/s41467-023-36643-5. [PubMed: 36806170]

66. Turner KL, Gheres KW, Proctor EA, and Drew PJ (2020). Neurovascular coupling and bilateral connectivity during NREM and REM sleep. Elife 9, e62071. 10.7554/eLife.62071.

67. Gerashchenko D, Schmidt MA, Zielinski MR, Moore ME, and Wisor JP (2018). Sleep State Dependence of Optogenetically evoked Responses in Neuronal Nitric Oxide Synthase-positive Cells of the Cerebral Cortex. Neuroscience 379, 189–201. 10.1016/j.neuroscience.2018.02.006. [PubMed: 29438803]

68. Yoshioka T, Nagaoka T, Song Y, Yokota H, Tani T, and Yoshida A. (2015). Role of neuronal nitric oxide synthase in regulating retinal blood flow during flicker-induced hyperemia in cats. Invest. Ophthalmol. Vis. Sci 56, 3113–3120. 10.1167/iovs.14-15854. [PubMed: 25783603]

69. Zhang HQ, Fast W, Marletta MA, Martasek P, and Silverman RB (1997). Potent and selective inhibition of neuronal nitric oxide synthase by N omega-propyl-L-arginine. J. Med. Chem 40, 3869–3870. 10.1021/jm970550g. [PubMed: 9397167]

70. Boer R, Ulrich WR, Klein T, Mirau B, Haas S, and Baur I. (2000). The inhibitory potency and selectivity of arginine substrate site nitric-oxide synthase inhibitors is solely determined by their affinity toward the different isoenzymes. Mol. Pharmacol 58, 1026–1034. [PubMed: 11040050]

71. Pigott B, Bartus K, and Garthwaite J. (2013). On the selectivity of neuronal NOS inhibitors. Br. J. Pharmacol 168, 1255–1265. 10.1111/bph.12016. [PubMed: 23072468]

72. Fenno LE, Mattis J, Ramakrishnan C, Hyun M, Lee SY, He M, Tucciarone J, Selimbeyoglu A, Berndt A, Grosenick L, et al. (2014). Targeting cells with single vectors using multiple-feature Boolean logic. Nat. Methods 11, 763–772. 10.1038/nmeth.2996. [PubMed: 24908100]

73. Lee JH, Durand R, Gradinaru V, Zhang F, Goshen I, Kim DS, Fenno LE, Ramakrishnan C, and Deisseroth K. (2010). Global and local fMRI signals driven by neurons defined optogenetically by type and wiring. Nature 465, 788–792. 10.1038/nature09108. [PubMed: 20473285]

74. Muntifering M, Castranova D, Gibson GA, Meyer E, Kofron M, and Watson AM (2018). Clearing for Deep Tissue Imaging. Curr. Protoc. Cytom 86, e38. 10.1002/cpcy.38. [PubMed: 30005145]

75. Hooks BM, Mao T, Gutnisky DA, Yamawaki N, Svoboda K, and Shepherd GMG (2013). Organization of cortical and thalamic input to pyramidal neurons in mouse motor cortex. J. Neurosci 33, 748–760. 10.1523/JNEUROSCI.4338-12.2013. [PubMed: 23303952]

76. Madisen L, Mao T, Koch H, Zhuo JM, Berenyi A, Fujisawa S, Hsu YWA, Garcia AJ 3rd, Gu X, Zanella S, et al. (2012). A toolbox of Cre-dependent optogenetic transgenic mice for light-induced activation and silencing. Nat. Neurosci 15, 793–802. 10.1038/nn.3078. [PubMed: 22446880]

Highlights

- Tacr1 neurons are long-range-projecting somatostatin neurons that co-express Nos1 and NPY
- Tacr1 neurons receive input from excitatory neurons and respond to sensory stimulation
- Tacr1 neurons are strong regulators of cerebral blood flow
- Tacr1 neurons regulate vasodilation via pericyte and vascular smooth muscle relaxation

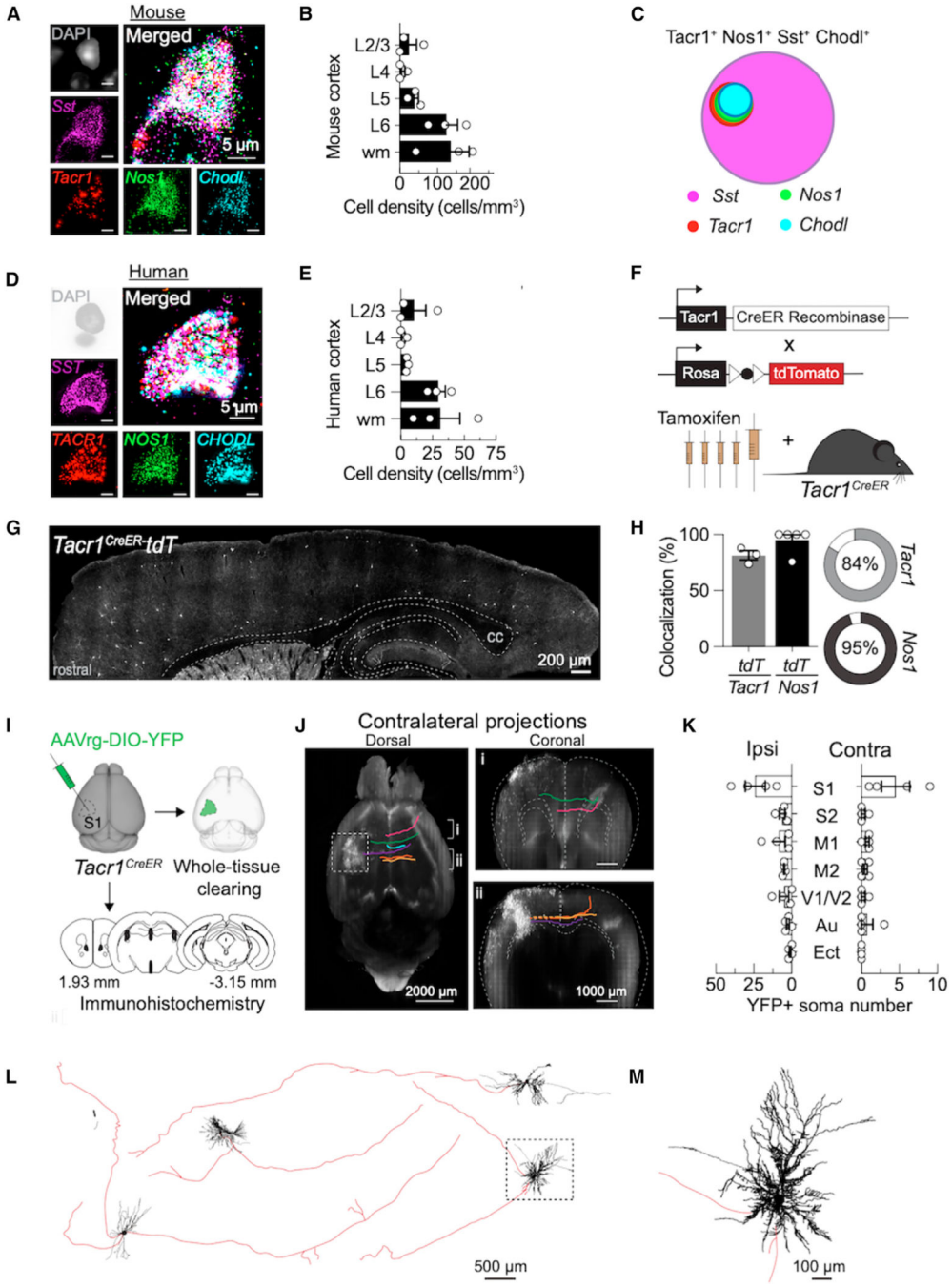

Figure 1. Tacr1 neurons are a conserved population of long-range GABAergic neurons

(A, B, D, and E) Representative multiplex fluorescence *in situ* hybridization (FISH) images demonstrating co-localization of *Sst/SST* (purple), *Tacr1/TACR1* (red), *Nos1/NOS1* (green), and *Chodl/CHODL* (blue) in cortical neurons in C57BL/6 mouse (A) and human (D). Scale bar, 5 µm. Quantification of neuronal density of quadruple-labeled cells in cortex and white matter (wm) in mouse (B, n = 3 mice) and human (E, n = 3 subjects).

(C) Venn diagram depicting the intersectionality of these neuronal populations in mouse (see also Figure S1).

(F) Cartoon depicting strategy to target Tacr1 neurons by crossing *Tacr1*^{CreER} mice to mice harboring a Cre-dependent tdTomato (tdT) fluorescent reporter.
(G) Representative sagittal section of Tacr1-mediated tdT expression in the mouse cortex after tamoxifen administration. Dashed lines are approximate anatomical borders. cc, corpus callosum. Scale bar, 200 μm.
(H) Quantification of the percentage of Tacr1- or Nos1-expressing neurons that expressed tdT (specificity) and the percentage of tdT^{+} neurons that co-expressed Tacr1 or Nos1 (recombination efficiency; see also Figure S2 and S3; n = 5 mice).[37]
(I) Schematic depicting experimental design. AAV-retrograde (rg) was injected into mouse somatosensory cortex. Brains were processed for whole-tissue clearing or IHC.
(J) Representative contralateral projections of traced Tacr1 neurons in dorsal (scale bar, 2000 μm) and coronal (scale bar, 1,000 μm) views of cleared brains (n = 6 cells from 2 mice).
(K) Quantification of Tacr1 neuron cell bodies in various brain regions following the injection AAVrg-DIO-YFP in *Tacr1*^{CreER} mice (n = 4).
(L) Representative neuronal reconstructions of tdT-labeled Tacr1 neurons from cleared brains showing long-range axons (red) and dendrites (black) (n = 4 cells).
(M) Inset from (L) (dashed square) to illustrate Tacr1 dendrites (see also Figure S4).
Data are mean ± SEM, error bars represent SEM, and dots represent data points from individual mice or subjects.

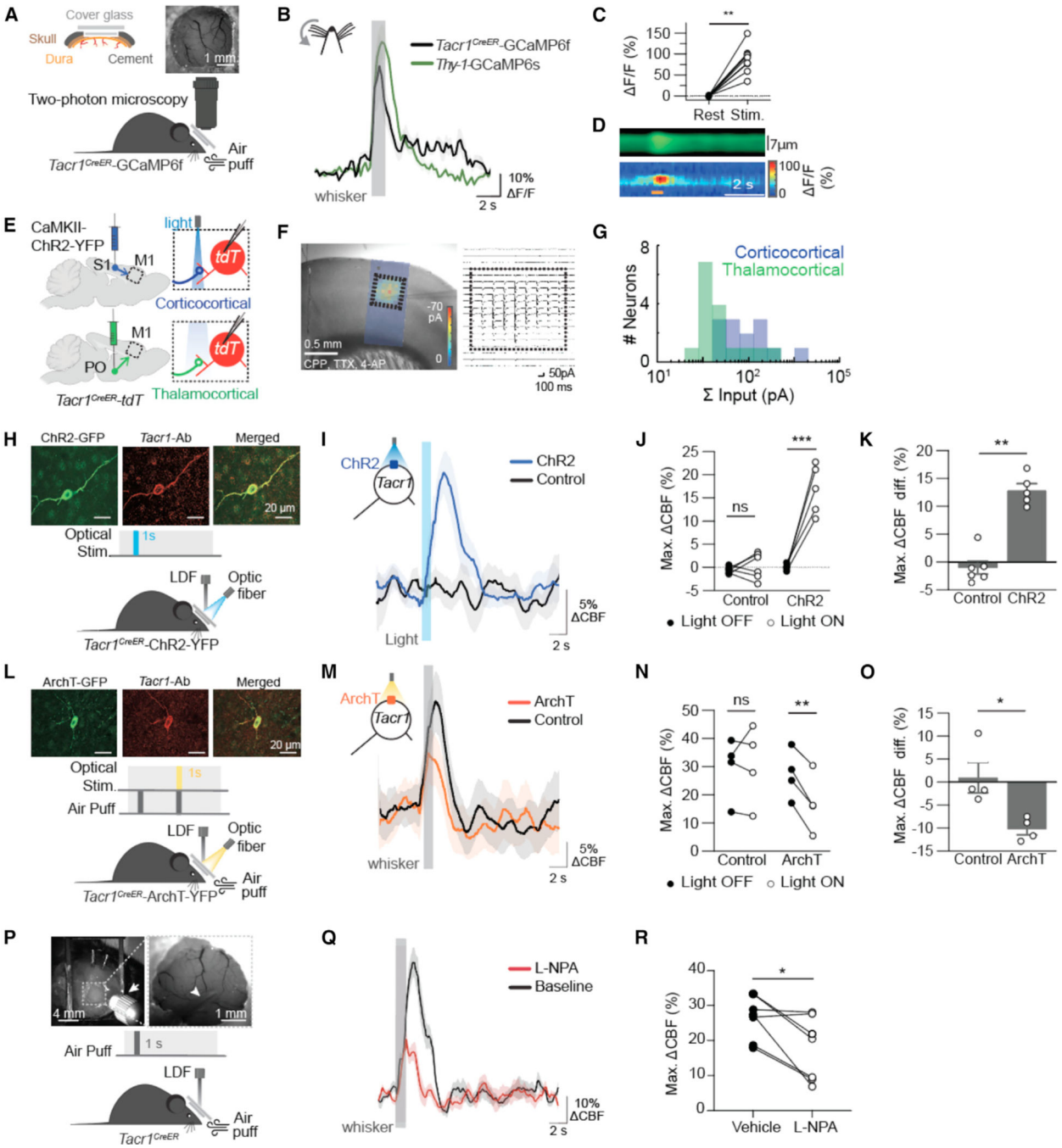

Figure 2. Tacr1 neurons are recruited for sensory-evoked NVC

(A) Top: schematic of chronic cranial window design and representative macroscopic image of a cranial window in mouse. Scale bar, 1 mm. Bottom: schematic depicting Ca^{2+} imaging by 2P microscopy in the S1 cortex. Sensory stimulation (air puff) to the contralateral whisker pad was performed to evoke a hemodynamic response.

(B) Time course of the percentage of change in Ca^{2+} signal (ΔF/F) in mice expressing GCaMP6f in Tacr1 neurons (black) or GCaMP6s in Thy1 (pyramidal) neurons (green) following sensory stimulation (10 trials per mouse).

(C) Maximum percentage of change in Ca^{2+} signal in mice expressing GCaMP6f in Tacr1 neurons before and after whisker stimulation (**p = 0.0039, n = 9 neurons in 5 mice).
(D) Representative line profiles showing changes in vessel diameter (μm) of a nearby vessel and ΔF/F (%) from a GCaMP6f-expressing Tacr1 neuron. Orange bar represents whisker stimulation (1 s, 50 Hz, 50 ms). Scale bar, 2 s.
(E) Left: schematic depicting strategy to express ChR2 in cortical (top) or thalamic (bottom) excitatory neurons. Areas outlined by the black dashed rectangle are shown at the right. Right: representation of ChR2-assisted circuit mapping (sCRACM) showing optogenetic stimulation of ChR2-expressing cortical or thalamic excitatory neurons and simultaneous recording from tdT-expressing Tacr1 neurons in the primary motor cortex (M1).
(F) Left: example sCRACM map superimposed on a bright-field image of an M1 brain slice. Scale bar, 0.5 mm. Right: example of averaged excitatory postsynaptic current ($EPSC_{sCRACM}$) recorded from the Tacr1 neuron displayed on the grid corresponding to the light stimulus location.
(G) Histogram of synaptic strength for cortical (S1, green; n = 13) and thalamic (PO, blue; n = 16) input to Tacr1 neurons in M1.
(H–K) Acute optogenetic excitation of cortical ChR2-expressing Tacr1 neurons. (H) Top: IHC showing co-localization of ChR2 (green) and Tacr1 (red) protein. Scale bar, 20 μm. Middle: optogenetic stimulation protocol (1 s, 5 Hz, 30 ms pulse width, blue light). Bottom: experimental setup demonstrating continuous CBF measurement by LDF during optical excitation in awake, head-fixed mice. (I) Representative time course of the change in CBF. (J) Maximum percentage of change in CBF from light OFF to ON in control mice (n = 6, 10 trials per mouse) and mice expressing ChR2 in Tacr1 neurons (n = 5 mice, 10 trials per mouse). Activation of cortical Tacr1 neurons significantly increased CBF relative to light OFF (***p = 0.0004) compared to control mice. (K) Difference in the maximum percentage of change in CBF between light OFF and light ON is increased in mice expressing ChR2 in Tacr1 neurons compared to control mice (**p = 0.0043; n =5 mice, 10 trials per mouse; see also Figure S5).
(L–O) Acute optogenetic silencing of cortical ArchT-expressing Tacr1 neurons. (L) Top: IHC showing co-localization of ArchT (green) and Tacr1 (red) protein. Scale bar, 20 μm. Middle: optogenetic silencing protocol (1 s, 5 Hz, 5 ms pulse width; yellow light). Bottom: experimental setup demonstrating continuous CBF recording by LDF during optical inhibition in the presence of sensory stimulation (air puff; 1 s, 10 Hz, 50 psi) in awake, head-fixed mice. (M) Representative time course of the change in CBF. (N) Maximum percentage of change in sensory-evoked CBF from light OFF to ON in mice expressing ArchT in Tacr1 neurons was significantly decreased compared to control mice (n = 4 mice, 10 trials per mouse, *p = 0.0038). Inhibition of cortical Tacr1 neurons significantly decreased sensory-evoked CBF relative to light OFF. (O) Difference in the maximum percentage of change in CBF between light ON and light OFF is significantly reduced in mice expressing ArchT in Tacr1 neurons compared to control mice (N, *p = 0.0143; n = 4 mice, 10 trials per mouse; see also Figure S6).
(P) Top: representative macroscopic image of cranial window with chronic cannula (arrow; scale bar, 4 mm) and the position of the LDF probe (arrowhead; scale bar, 1 mm). Middle: sensory stimulation protocol (air puff; 1 s, 5 Hz, 50 psi). Bottom: experimental setup

demonstrating continuous CBF recording by LDF during sensory stimulation in awake, head-fixed mice.

(Q) Representative time course of the change in CBF following whisker stimulation before (baseline; black) and after (red) cortical infusion of an nNOS inhibitor (1 μL, 1 mM) through the chronic cannula.

(R) Difference in the maximum percentage of change in sensory-evoked CBF 30 min after infusing L-NPA, a nNOS inhibitor, was significantly decreased relative to vehicle (1× PBS, 1 μL) (n = 7 mice, 10 trials per mouse, *p = 0.0179).

Data are mean ± SEM. Statistical significance was determined by paired, nonparametric two-tailed t test (C); paired, parametric, two-tailed t test (J, N, and R); or unpaired, nonparametric two-tailed t test (K and O). ns, not significant. Error bars and shaded areas are SEM.

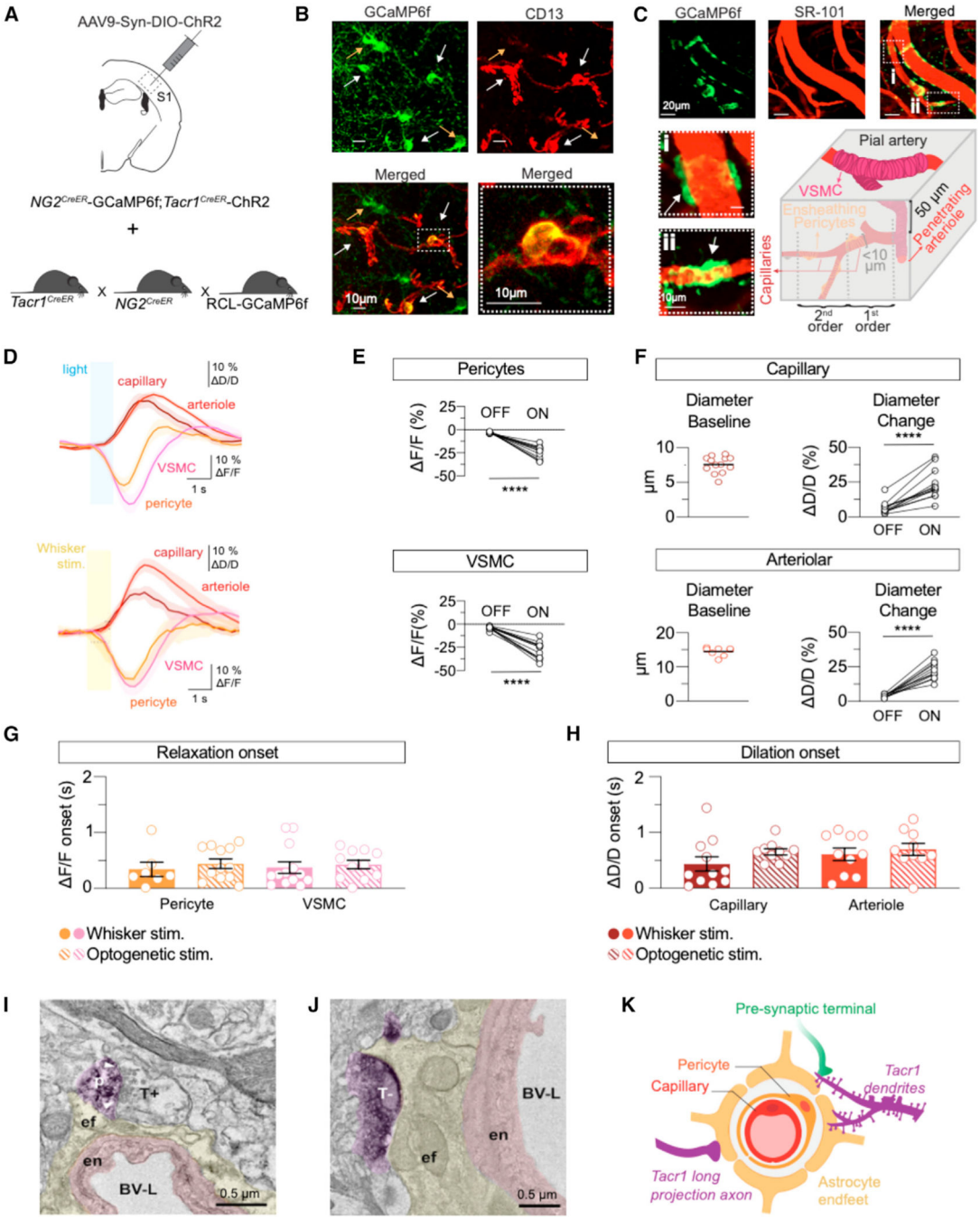

Figure 3. Tacr1-neuron-evoked NVC is mediated by contractile ensheathing pericytes and arteriolar VSMCs

(A) Schematic depicting strategy to express ChR2 in Tacr1 neurons and GCaMP6f in NG2 mural cells (note: with this strategy, GCaMP6f is also expressed in Tacr1 neurons, although it is not relevant in these experiments).

(B) White arrows indicate ensheathing pericytes that express GCaMP6f (green) and CD13 (pericyte marker, red). Yellow arrows indicate cells that only express GCaMP6f (green). Scale bar, 10 μm.

(C) Top: representative *in vivo* 2P image (maximum intensity projection) showing GCaMP6f-expressing VSMCs (green) and SR-101-labeled vasculature (red). In merged image, white dashed boxes are shown enlarged at the bottom. Scale bar, 20 μm. Bottom: a VSMC (white arrow) on arteriole (i) and an ensheathing pericyte (white arrowhead) on capillary (ii). Scale bar, 10 μm. Cartoon depicts vascular tree denoting VSMCs surrounding arterioles as well as ensheathing pericytes surrounding capillaries, VSMCs/pericytes, and vascular dynamics upon optogenetic stimulation in Tacr1 neurons and whisker stimulation (n = 7–13 measurements from 5 mice).

(D) Top: time course of the change in average VSMC/pericyte Ca^{2+} signal and subsequent vessel diameter upon either optogenetic stimulation (10 trials) of Tacr1 neurons (top) or whisker stimulation (bottom).

(E) Maximum percentage of change in pericyte (top) and VSMC (bottom) Ca^{2+} signal (ΔF/F, ****$p < 0.0001$, 12 pericytes and 13 VSMCs).

(F) Baseline diameter and maximum percentage of change in capillary (top) and arteriolar (bottom) diameter (ΔD/D, ****$p < 0.0001$, 12 capillaries and 12 arterioles).

(G and H) Latency to onset of (G) mural cell relaxation or (H) vascular dilation upon either optogenetic stimulation (n = 12 pericytes, 11 VSMCs, 10 capillaries, 10 arterioles) or whisker stimulation (n = 7 pericytes, 13 VSMCs, 11 capillaries, 10 arterioles) (see also Figure S7).

(I) Representative image of Tacr1 dendritic spine (purple) forming an asymmetrical synapse with a putative excitatory terminal (T+). White arrowheads point out the edges of the postsynaptic density (p). The Tacr1 distal dendrite receiving a putative excitatory terminal (T+) also contacts the perivascular astrocyte endfoot (ef; yellow), forming a suspected neuronal-astrocytic-vascular tripartite functional unit. Scale bar, 0.5 μm.

(J) Tacr1 putative inhibitory axon terminal (T−) contacting astrocytic endfeet. en, endothelial cell; BV-L, blood vessel lumen. Scale bar, 0.5 μm.

(K) Schematic of the neurovascular unit including proposed perivascular location of Tacr1 processes (see also Figure S8).

Data are mean ± SEM. Statistical significance was determined by paired, parametric two-tailed t test (E and F) or unpaired, two-tailed Mann-Whitney test (G and H). Error bars and shaded areas are SEM.

KEY RESOURCES TABLE

REAGENT or RESOURCE	SOURCE	IDENTIFIER
Antibodies		
Rabbit poiycionai anti-GFP	Thermo Fisher Scientific	Cat# A-11122, RRID: AB_221569
Rabbit polyclonal anti-Substance P Receptor	Sigma-Aldrich	Cat# SB305, Accession# P25103, RRID: AB_261562
Goat polyclonal anti-nNOS	Abcam	Cat# ab1376, RRID: AB_300614
Rabbit polyclonal anti-Neuropeptide Y	Peninsula Laboratories, LLC	Cat# T-4070, UniProt Code P01303, RRID: AB_518504
Goat polyclonal anti- Parvalbumin	Swant	Cat# PVG-213, RRID: AB_2650496
Rabbit polyclonal anti-RFP	Rockland	Cat# 600-401-379S, UniProt Code Q9U6YB, RRID: AB_11182807
Rabbit polyclonal anti-Somatostatin	Peninsula Laboratories, LLC	Cat# T-4547, RRID: AB_518618
Goat anti-rabbit, Alexa Fluor 488	Thermo Fisher Scientific	Cat# A-11034, RRID: AB_2576217
Goat anti-rabbit, Aiexa Fiuor 555	Thermo Fisher Scientific	Cat# A-2142B, RRID: AB_2535849
Donkey anti-goat, Alexa Fluor 488	Thermo Fisher Scientific	Cat# A-11055, RRID: AB_2534102
DAPI	Advanced Cell Diagnostics, ACD	Cat# 320B5B
Biotinylated goat anti-rabbit IgG secondary antibody	Vector labs	Cat# CY-1500 and CY-1500-1, RRID: AB_2868518
Bacterial and virus strains		
AAVr.EF1a.DIO.hChR2(H134R).EYFP-WPRE-HGH	Kari Deisseroth Lab	Addgene #20298-AAVr
AAV5-hSyn-Con/Foff-hChR2(h134R)-EYFP	Fenno et ai.[72]	Addgene #55646-AAV5
AAV9-CaMKIIa-hChR2(H134R)-EYFP	Lee et ai.[73]	Addgene #26969-AAV9
Bioiogicai sampies		
Healthy adult brain tissue	Translational Neuroscience Program's brain bank, Department of Psychiatry, University of Pittsburgh	N/A
Chemicais, peptides, and recombinant proteins		
Tamoxifen	Sigma-Aldrich	SKU T564B
Corn oil	Sigma-Aldrich	Cat# CB267-500ML
Normal goat serum	Jackson ImmunoResearch	Code: 005-000-121, RRID: AB_2336990
Normal donkey serum	Jackson ImmunoResearch	Code: 017-000-121, RRID: AB_233725B
Prolong Diamond AntiFade	Thermo Fisher Scientific	P36961
Tetrodotoxin (TTX)	Abcam	ab120055
4-Aminopyridine	Sigma-Aldrich	SKU 275B75
Isoflurane	Henry Schein	Cat# 11B209B
Dental cement	Stoelting Co.	Cat# 5145B
Sulforhodamine 101	Thermo Fisher Scientific	Cat# S359
Nω-Propyi-L-arginine hydrochioride	Tocris	Cat# 1200

REAGENT or RESOURCE	SOURCE	IDENTIFIER
Fluoromount-G	SouthernBiotech	Cat# 0100-01
Epoxy resin	Electron Microscopy Science	EMS #14120
O.C.T. Compound	Thermo Fisher Scientific	Cat# 23-730-571
Dental Cement Kit, Pink Opaque	Stoelting Co.	Cat# 5145B
Ketofen (Ketoprofen)	Covetrus	SKU: 0054B7
Buprenex (Buprenorphine)	Par Pharmaceutical, Inc	NDC: 42023-0179-05
Bupivacaine HCl 0.5%	Covetrus	SKU: 062076
Critical commercial assays		
RNAscope Multiplex Fluorescent v1 Assay	Advanced Cell Diagnostics, ACD	Cat# 320850
RNAscope Multiplex Fluorescent v2 Assay	Advanced Cell Diagnostics, ACD	Cat# 320850
Elite ABC (Avidin-Biotin Complex)-HRP Kit	Vector Laboratories	PK-6200
DAB Substrate Kit, Peroxidase (HRP), with Nickel, (3,3′-diaminobenzidine)	Vector Laboratories	SK-4100
Deposited data		
Custom code for experiments	This paper	https://zenodo.org/doi/10.5281/zenodo.10656013
Custom code for data analysis with processed data	This paper	https://doi.org/10.5281/zenodo.10671436
Experimental models: Organisms/strains		
Mouse: C57BL/6J	Charles River	no. 027
Mouse: Tacr1 $^{tm11(cre/ERT2)sros/j}$	The Jackson Laboratory	JAX 035046
Mouse: B6.Cg-Tg(Cspg4-cre/Esr1*)BAkik/J	The Jackson Laboratory	JAX 008538
Mouse: B6.Cg-*Gt(ROSA)26Sor*$^{tm9(CAG\_tdTomato)Hze}$/J	The Jackson Laboratory	JAX 007909
Mouse: B6; 129S-*Gt(ROSA)26Sor*$^{tm32(CAG\_COP4*H134R/EYFP)Hze}$/J	The Jackson Laboratory	JAX 012569
Mouse: B6; 129S-Gt(ROSA)26Sortm35.1(CAG-aop3/GFP)Hze/J	The Jackson Laboratory	JAX 012735
Mouse: B6J.Cg-Gt(ROSA)26Sor$^{tm95.1(CAG-GCaMP6f)Hze}$/MwarJ	The Jackson Laboratory	JAX 028865
Mouse: C57BL/6J-Tg(Thy1-GCaMP6s)GP4.3Dkim/J	The Jackson Laboratory	JAX. 024275
Oligonucleotides		
Mm-Tacr1	Advanced Cell Diagnostics, ACD	Cat# 428781
Mm-tdTomato	Advanced Cell Diagnostics, ACD	Cat# 317041
Mm-Nos1	Advanced Cell Diagnostics, ACD	Cat# 437651
Mm-Chodl	Advanced Cell Diagnostics, ACD	Cat# 450211
Mm-Sst	Advanced Cell Diagnostics, ACD	Cat# 404631
Hu-TACR1	Advanced Cell Diagnostics, ACD	Cat# 17166A
Hu-NOS1	Advanced Cell Diagnostics, ACD	Cat# 171594
Hu-CHODL	Advanced Cell Diagnostics, ACD	Cat# 171634
Hu-SST	Advanced Cell Diagnostics, ACD	Cat# 17145C
RNAscope™ DAPI	Advanced Cell Diagnostics, ACD	Cat# 320858

REAGENT or RESOURCE	SOURCE	IDENTIFIER
Software and algorithms		
MATLAB R2019a or 2020	Mathworks	https://ww2.mathworks.cn/
Imaris v9.7.2	Imaris	https://imaris.oxinst.com/
Graphpad Prism	GraphPad Software	Version 9
Ephus	Ephus software	www.ephus.org
ImageJ	Schneider et al.[37]	https://imagej.net/ij/
Other		
Laser (473/589 nm)	CrystaLaser, Inc.	N/A
Optic fiber 125 μm diameter	ThorLabs, Inc.	S-405-HP
TTL-controlled laser diode unit	CrystaLaser, Inc.	N/A
Core Multimode Optical Fiber 200 μm diameter	ThorLabs, Inc.	FT200EMT
Axopatch 700B	Molecular Devices	N/A
CUBIC R1	Muntifering et al.[74]	N/A
CUBIC R2	Muntifering et al.[74]	N/A
Confocal microscopy	Nikon A1R	N/A
Fluorescent microscopy	Nikon 90i	N/A
Leica EM UC7 Ultramicrotome	Leica Microsystems	N/A
JEOL-1400 transmission electron microscope	JEOL Ltd.	N/A
Orius™ SC200 CCD camera	Gatan Inc.	N/A
Small Animal Stereotaxic Instrument	Kopf Instruments	Model 942
Stainless-steel burr	Fine Science Tools	Item# 19008-07
High Speed Rotary Micromotor Kit	Foredom Electric Co.	SKU K1070
3.5 in. Glass Capillaries	Drummond Scientific Company	Cat# 3-000-203-G/X
Nanoinjector III	Drummond Scientific Company	Cat.#3-000-207
RS-G4 Upright Research Confocal Microscope	Caliber ID	N/A
Custom-built laser scanning photostimulation microscope	Hooks lab[75]	N/A
Aluminum chamber frame	Narishige Inc.	CF-10
Small round cover glass, 4 mm, CS-4R	Warner Instruments Inc.	Cat# 64-0724
Small round cover glass, 5 mm, CS-5R	Warner Instruments Inc.	Cat# 64-0700
Ortho-Jet™ Powder	Lang Dental Manufacturing Company	Item#: 1320CLR
Ortho-Jet BCA Liquid	Lang Dental Manufacturing Company	Item#: Ortho-Jet BCA Liquid
Head Holder Plate	Narishige Inc.	MAG-1
Custom treadmill	Vazquez lab	N/A
Guide Cannula-Single/OD0.41mm-27G/M3.5	RWD Life Science Inc.	Cat# 62004
Injector-Single/OD0.21mm-33G	RWD Life Science Inc.	Cat# 62204
Dust Cap(Alu)-Single/OD0.20mm/M3.5	RWD Life Science Inc.	Cat# 62108
Bulk Catheter 22, PU, IDxOD = 0.61 × 1.02mm, fits 22ga	RWD Life Science Inc.	Cat# BC-22
One Channel Programmable Syringe Pump	New Era Pump Systems Inc.	Model: NE-1002X
3M Vetbond Tissue Adhesive	Fisher Scientific	Cat# NC0735004

REAGENT or RESOURCE	SOURCE	IDENTIFIER
Toohey Spritzer Pressure System	Toohey Company	N/A
MP150 system	Biopac Systems Inc.	MP150
LDF Periflux 5000/411	Perimed AB	N/A
Ultima IV microscope	Bruker Nano Analytics	N/A
Ultra-fast laser Excite X3	Newport Spectra-Physics, Inc	N/A
National Instruments board PCI-6601	National Instruments Corp.	N/A